Applied Mathematical Modelling 150 (2026) 116327

Contents lists available at ScienceDirect

Applied Mathematical Modelling

journal homepage: www.elsevier.com/locate/apm

Variationally consistent Maxwell stress in flexoelectric structures under finite deformation and immersed in free space

Xiaoying Zhuang [a,b,*], Han Hu [a,**], S.S. Nanthakumar [a], Quoc-Thai Tran [c], Yanpeng Gong [a,d], Timon Rabczuk [e]

[a] Institute of Photonics, Faculty of Mathematics and Physics, Leibniz University Hannover, Hannover, 30167, Germany
[b] College of Civil Engineering, Department of Geotechnical Engineering, Tongji University, Shanghai, 20092, China
[c] Fluid Dynamics and Solid Mechanics, T-3, Theoretical Division, Los Alamos National Laboratory, Los Alamos, NM 87545, USA
[d] Institute of Electronics Packaging Technology and Reliability, Faculty of Materials and Manufacturing, Beijing University of Technology, Beijing 100124, China
[e] Institute of Structural Mechanics, Bauhaus University Weimar, 99423 Weimar, Germany

ARTICLE INFO

Keywords:
Flexoelectricity
Maxwell stress
Free space
Finite deformation
Isogeometric analysis
Bursting drop

ABSTRACT

Maxwell stress refers to the mechanical stress exerted on a dielectric material due to the presence of electric fields. It plays a significant role in the interaction between a dielectric material and the surrounding free space under finite deformation. Previous research on finite deformation of flexoelectricity mainly adopted a modified form of Maxwell stress, potentially not able to correctly capture some physical phenomena, such as the compression of a dielectric droplet in an electric field. In this work, we propose a consistent and complete variational principle for flexoelectricity, in which the Maxwell stress emerges naturally from the derivation, without introducing additional assumptions. An Isogeometric analysis-based numerical framework is developed accordingly and verified by both linear and nonlinear benchmark cases compared with experimental results. The present framework successfully captures and quantifies the behaviors of conductive liquids and soft dielectric solids subjected to an external electric field. Finally, a novel scenario is investigated in which a flexoelectric beam immersed in free space is analyzed, showing the interesting distribution of Maxwell stress-induced tractions at opposing boundaries. The test demonstrates that a higher dielectric constant can effectively enhance the material's stiffness in response to the external electric loading.

1. Introduction

Flexoelectricity, the electro-mechanical coupling effect between electric field and strain gradient (or strain and electric field gradient), has gained prominence as electronic and mechanical devices continue to shrink while demanding higher efficiency [1]. Unlike piezoelectricity, which appears only in noncentrosymmetric crystals, flexoelectricity is inherent to every dielectric because a strain gradient locally breaks inversion symmetry. Experimental studies cover a wide spectrum of materials. Substantial flexoelectric coefficients have been measured in hard ferroelectric perovskites such as barium titanate and lead zirconate titanate [2]. Two dimensional

* Corresponding author at: Institute of Photonics, Faculty of Mathematics and Physics, Leibniz University Hannover, Hannover, 30167, Germany.
** Corresponding author, contributed equally to this work.
E-mail addresses: zhuang@iop.uni-hannover.de (X. Zhuang), hanhu@iop.uni-hannover.de (H. Hu).

https://doi.org/10.1016/j.apm.2025.116327
Received 22 March 2025; Received in revised form 10 July 2025; Accepted 21 July 2025

Available online 31 July 2025

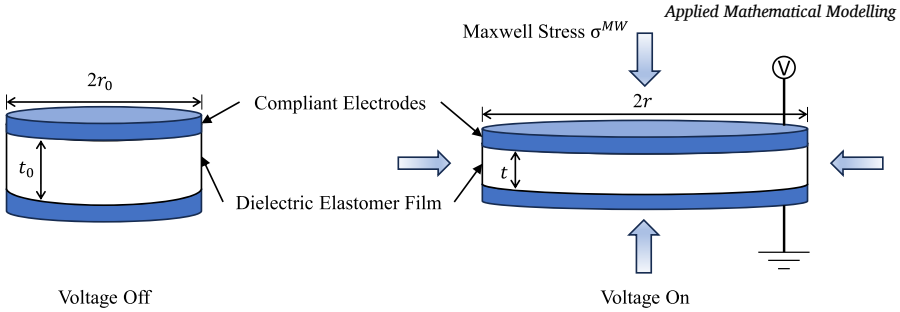

Fig. 1. Schematic of Maxwell stress effect.

Table 1
Representative formulations of the Maxwell stress tensor; ϵ_0: vacuum permittivity, e_i: electric field, d_i: electric displacement.

Proposer	Maxwell stress tensor $\sigma_{ij}^{\mathrm{MW}}$
Lorentz [33]	$\epsilon_0 e_i e_j - \frac{1}{2}(\epsilon_0 e_i e_i)\delta_{ij}$
Einstein and Laub [36]	$e_i d_j - \frac{1}{2}(\epsilon_0 e_i e_i)\delta_{ij}$
Minkovski [34]	$e_i d_j - \frac{1}{2}(e_i d_i)\delta_{ij}$
Abraham [35]	$\frac{1}{2}(e_i d_j + e_j d_i) - \frac{1}{2}(e_i d_i)\delta_{ij}$

sheets, for example hexagonal boron nitride, also display pronounced responses [3]. In soft matter the effect can be even stronger. Liquid crystals [4], polymer films [5], and biological membranes [6] all produce sizable polarization when bent or otherwise deformed. Because soft dielectrics combine large, reversible deformation with strong electromechanical coupling, they are attractive for practical devices. Recent prototypes include artificial muscles and grippers for soft robotics [7], skin-conforming pressure sensors [8], and energy harvesters [9].

Modeling flexoelectricity is crucial for understanding and predicting corresponding physical phenomena. Continuum theories of flexoelectricity, originating from early works of Toupin [10] and Mindlin [11] on elastic dielectrics, have developed over the years [12–17]. An overview on the mathematical modeling of flexoelectricity can be found in [18]. To address finite deformation in soft materials, a nonlinear framework is essential. However, few related works have emerged only recently [19–26]. The existing literature on modeling nonlinear flexoelectricity generally encounters two common limitations. The first, as argued in [23], is the loss of objectivity in defining polarization, which arises from using a mixed material-spatial coupling tensor to represent work done by flexoelectricity. The second limitation concerns the accurate quantification of Maxwell stress, which must be consistent with the variational principle in use. Maxwell stress refers to the stress exerted in a medium (dielectric or free space) due to electric fields [27]; magnetic field effects are not considered in this work. As schematically depicted in Fig. 1, a dielectric elastomer film deforms when exposed to the electric field created by applying a voltage via the electrodes attached to it. Maxwell stress has been identified as responsible for the deformation in this case and has been reported in many works [28–30]. While negligible under infinitesimal assumptions [20], it is of great importance in finite deformation, especially when considering the interaction with the surrounding medium [31].

In electrodynamics [32], there are various proposals for the formulation of the Maxwell stress tensor. The version proposed by Lorentz [33] applies to free space and is generally undisputed. The central issue, known as the 'Abraham–Minkowski controversy', arises from the fact that several distinct and non-equivalent formulations were proposed for ponderable (solid or fluidic) matter, most notably by Minkowski [34], Abraham [35], and Einstein and Laub [36]. These four representative forms of the Maxwell stress tensor are summarized in Table 1. While all of these formulations become equivalent in a vacuum, they predict different local body forces and surface tractions within a dielectric medium, leading to a long-standing debate over which is the most accurate. At present, Minkovski's form is the generally accepted definition of the Maxwell stress tensor in solid mechanics [37]. In electroelasticity, the Maxwell stress can be fully determined through the variational principle when the system behavior can be characterized by a total energy functional. This principle also applied in related fields, such as the electrohydrodynamics of fluids [38]. In [19,21,22], the expression for Maxwell stress is adopted from a modified version, potentially inconsistent with the variational principle. Therefore, some physical phenomena cannot be correctly captured, such as the compression of a dielectric in an electric field. In contrast, the Maxwell stress defined in [23] is presented partially without taking into account all contributions of flexoelectricity. Therefore, deriving governing equations with a variationally consistent Maxwell stress fulfilling a complete variational principle is necessary to both form a solid theory of flexoelectricity and correctly simulate correlated physical phenomena.

The influence of free space is often overlooked in simulations of dielectric materials, particularly for structures with significantly smaller thickness compared with their other dimensions [39]. However, for materials with a weak dielectric constant, such as those only one order greater than that of vacuum [40], the contribution of the free space may become significant. This influence is not limited to the distribution of electric potential within the dielectric solid; it also includes the exertion of a traction force on the body's boundary due to Maxwell stress in free space, a crucial aspect for the functioning of some electro-active devices [41]. Free space is studied for general dielectrics in 2D [42] and 3D [43] through a coupled BEM-FEM approach, mixed variational formulation [39] with

mesh update method, and for topology optimization of electro-active polymers [44]. Research on flexoelectric materials interacting with free space, however, remains limited. While this topic is addressed in [21] and [22], flexoelectricity does not appear to play a significant role in the test examples they used.

Computational modeling of flexoelectricity necessitates numerical methods that guarantee the smoothness of strain within the domain of the dielectric solid, specifically ensuring the C^1 continuity of the state variables. Various numerical approaches have been proposed, including the mesh-free method [45–48], the mixed Finite Element method [24,49–52], and Isogeometric analysis [22,23,53,54]. An extensive overview of the computational methods is available in [55], which compares the effectiveness of these three methods. Other numerical methods include C^1-continuous Argyris-triangle-based finite element method [21], B-spline-based immersed boundary method [56] and micromorphic fields approach [57,58].

The main contributions of this study are threefold: (i)We derive an explicit Maxwell stress tensor that is fully consistent with a total-Lagrangian energy functional and embeds the flexoelectric contribution. (ii) The finite deformation flexoelectric framework is generalized to include the electrostatic energy stored in the surrounding free space, enabling body–environment coupling. (iii) A C^1-continuous NURBS formulation accurately reproduces standard benchmarks and captures bursting-drop evolutions, offering new insights into how dielectric permittivity governs the mechanical compliance of soft flexoelectric materials. These advances provide a rigorous foundation for practical systems such as soft-robotic actuators, flexoelectric sensors and micro-energy harvesters, and electromechanically tunable metamaterials operating in free space. The paper is structured as follows. Section 2 introduces a complete variational principle for a flexoelectric body immersed in free space, formulating strong governing equations in both electrical and mechanical aspects, and deriving the variationally consistent Maxwell stress in an explicit form. Section 3 establishes and linearizes the weak form formulation to facilitate numerical implementation. In Section 4, two benchmark cases, namely the cantilever beam and the truncated pyramid, are examined to validate the proposed numerical framework. Section 5 demonstrates the capability of the nonlinear flexoelectricity model in simulating problems involving finite deformation, using a cantilever beam subjected to mechanical or electrical loadings as examples. Finally, Section 6 explores the influence of free space using a well-established model, and presents a new study of a flexoelectric beam immersed in free space.

2. Variational principle

2.1. Background information

Consider a deformable dielectric solid represented by $\mathcal{B}_0$ in the reference or undeformed configuration, immersed by the surrounding free space represented by $\mathcal{B}_0'$. Their corresponding representations in the current or deformed configuration are respectively $\mathcal{B}$ and $\mathcal{B}'$. The whole space of concern is $V_0 = \mathcal{B}_0 \cup \mathcal{B}_0'$ and $V_t = \mathcal{B} \cup \mathcal{B}'$. The boundary of $\mathcal{B}_0$ is denoted as $\partial\mathcal{B}_0$ and coincide with $\partial\mathcal{B}_0'$ in the near field, while $\partial\mathcal{B}_\infty'$ represents the bound of the free space in the far field. The deformation map $\chi : V_0 \to V_t$ maps every material point $\boldsymbol{X} \in V_0$ to the spatial point $\boldsymbol{x} = \chi(\boldsymbol{X}) \in V_t$. Uppercase and lowercase notations are used to refer to quantities in the reference and current configurations throughout the paper. The deformation gradient tensor $\mathbf{F}$, Jacobian determinant J are defined as

$$F_{iI}(\boldsymbol{X}) := \frac{\partial \chi_i(\boldsymbol{X})}{\partial X_I} = \chi_{i,I}, \quad J := \det(\mathbf{F}), \tag{1}$$

and the right and left Cauchy-Green deformation tensor $\mathbf{C}$ and $\mathbf{B}$ are defined as

$$C_{IJ} := F_{kI}F_{kJ}, \quad B_{ij} := F_{iK}F_{jK}, \tag{2}$$

where Einstein summation convention has been adopted for dummy indices. The Green-Lagrangian strain tensor $\boldsymbol{\mathcal{E}}$ for the reference configuration and the Almansi-Eulerian strain tensor $\boldsymbol{\epsilon}$ for the current configuration are defined as

$$\boldsymbol{\mathcal{E}} := \frac{1}{2}(C_{IJ} - \delta_{IJ}), \quad \boldsymbol{\epsilon} := \frac{1}{2}(\delta_{ij} - B_{ij}^{-1}). \tag{3}$$

Flexoelectricity theory involves the measure of strain gradient in the material, which entails the gradient of the deformation gradient $\boldsymbol{\mathcal{F}}$, the gradient of the Cauchy-Green deformation tensor $\boldsymbol{\mathcal{C}}$, and the Green-Lagrangian strain gradient tensor $\boldsymbol{\mathcal{G}}$, represented as [23]

$$\mathcal{F}_{iJK} := \frac{\partial F_{iJ}}{\partial X_K} = \chi_{i,JK}, \quad \mathcal{C}_{IJK} := \frac{\partial C_{IJ}}{\partial X_K} = 2\underset{IJ}{\text{symm}}(\mathcal{F}_{kIK}F_{kJ}), \quad \mathcal{G}_{IJK} := \frac{\partial \mathcal{E}_{IJ}}{\partial X_K} = \frac{1}{2}C_{IJK}, \tag{4}$$

where $\text{symm}_{IJ}(A_{IJ}) := (A_{IJ} + A_{JI})/2$. Their Eulerian counterparts can be obtained similarly as

$$\mathcal{F}_{Ijk}^{-1} := \frac{\partial F_{Ij}^{-1}}{\partial x_k} = X_{I,jk}, \quad \mathcal{B}_{ijk}^{-1} := \frac{\partial B_{ij}^{-1}}{\partial x_k} = 2\underset{ij}{\text{symm}}(\mathcal{F}_{Kik}^{-1}F_{Kj}^{-1}), \quad g_{ijk} = \frac{\partial \varepsilon_{ij}}{\partial x_k} = -\frac{1}{2}\mathcal{B}_{ijk}^{-1}. \tag{5}$$

The work conjugate to $\boldsymbol{\mathcal{E}}$ is the so-called second Piola-Kirchhoff stress tensor $\mathbf{S}$, which relates to the Cauchy stress $\boldsymbol{\sigma}$ (work conjugate to $\boldsymbol{\epsilon}$) by

$$S_{IJ} = JF_{Ii}^{-1}F_{Jj}^{-1}\sigma_{ij}. \tag{6}$$

Next, we introduce variables related to the electricity denoted by $\boldsymbol{E}$, $\boldsymbol{D}$ and $\boldsymbol{P}$, respectively, the electric field, the electric displacement and the polarization in the reference configuration, and $\boldsymbol{e}$, $\boldsymbol{d}$ and $\boldsymbol{p}$ are their counterparts in the current configuration. Derived from

the Maxwell's equations in the absence of magnetic interactions, distributed charges and time dependence, the following equations are satisfied as

$$\nabla \times \boldsymbol{e} = \boldsymbol{0}, \quad \nabla \cdot \boldsymbol{d} = 0. \tag{7}$$

The first equation of (7) implies the existence of an electric potential field ϕ such that $\boldsymbol{e} = -\nabla\phi$. The polarization vector is considered as a derived quantity in terms of $\boldsymbol{e}$ and $\boldsymbol{d}$ by the standard equation

$$\boldsymbol{p} = \boldsymbol{d} - \epsilon_0 \boldsymbol{e}, \tag{8}$$

where ϵ_0 is the dielectric constant of air or vacuum. Denote the space split by $\partial\mathcal{B}$ as side '+' and side '−', assuming the absence of free surface charge, the continuity conditions for $\boldsymbol{e}$ and $\boldsymbol{d}$ are given by

$$\boldsymbol{n} \times [\![\boldsymbol{e}]\!] = 0, \quad \boldsymbol{n} \cdot [\![\boldsymbol{d}]\!] = 0 \quad \text{on } \partial\mathcal{B}, \tag{9}$$

where $[\![\bullet]\!] = (\bullet)_+ - (\bullet)_-$ is the jump of the vector on $\partial\mathcal{B}$ from side − to side + with $\boldsymbol{n}$ the unit normal vector on $\partial\mathcal{B}$ pointing from side '−' to side '+'.

The electric potential can also be expressed in the Lagrangian frame as $\Phi(\boldsymbol{X}) = \phi(\chi(\boldsymbol{X}))$, from which the relation between $\boldsymbol{E}$ and $\boldsymbol{e}$ can be established using the chain rule as

$$E_L = -\frac{\partial \Phi}{\partial X_L} = -\Phi_{,L} = -\Phi_{,k}\, \chi_{k,L} = e_k F_{kL}. \tag{10}$$

The relation between $\boldsymbol{D}$ and $\boldsymbol{d}$ can be found by the work-conjugacy $d_l e_l = \frac{1}{J} D_L E_L$, such that

$$D_L = J F^{-1}_{Lk} d_k. \tag{11}$$

As discussed in [23], the polarization vector defined in a complete Lagrangian frame should have the same relation with its Eulerian counterpart as (11) to ensure objectivity, denoted by

$$P_L = J F^{-1}_{Lk} p_k. \tag{12}$$

The Eulerian equations (7) can be transferred into their Lagrangian counterparts provided a sufficiently regular deformation as

$$\nabla \times \boldsymbol{E} = \boldsymbol{0}, \quad \nabla \cdot \boldsymbol{D} = 0. \tag{13}$$

The jump conditions can be analogously written with respect to their Eulerian counterpart (9) as

$$\boldsymbol{N} \times [\![\boldsymbol{E}]\!] = 0, \quad \boldsymbol{N} \cdot [\![\boldsymbol{D}]\!] = 0 \quad \text{on } \partial\mathcal{B}_0, \tag{14}$$

where $\boldsymbol{N}$ is the unit normal vector on $\partial\mathcal{B}_0$, which relates to $\boldsymbol{n}$ by Nanson's formula as

$$\boldsymbol{n}\mathrm{d}a = J\mathbf{F}^{-\mathrm{T}}\boldsymbol{N}\mathrm{d}A, \tag{15}$$

where an area element $\mathrm{d}A$ on $\partial\mathcal{B}_0$ relates to an area element $\mathrm{d}a$ on $\partial\mathcal{B}$.

2.2. Lagrangian electric Gibbs free energy density formed by constitutive relations

We derived our formulations followed the procedure proposed by Codony et al. [23]. The Lagrangian internal energy density per unit reference volume for a dielectric without assuming its symmetry, i.e. flexoelectric and piezoelectric effects may co-exist, can be expressed as

$$\Psi^{\mathrm{Int}}(\boldsymbol{\mathcal{E}}, \boldsymbol{\mathcal{G}}, \boldsymbol{P}) = \Psi^{\mathrm{Mech}}(\boldsymbol{\mathcal{E}}, \boldsymbol{\mathcal{G}}) + \Psi^{\mathrm{Diele}}(\boldsymbol{\mathcal{E}}, \boldsymbol{P}) + \Psi^{\mathrm{Flexo}}(\boldsymbol{\mathcal{G}}, \boldsymbol{P}) + \Psi^{\mathrm{Piezo}}(\boldsymbol{\mathcal{E}}, \boldsymbol{P}), \quad \text{in } \mathcal{B}_0. \tag{16}$$

The first term of (16) shows the mechanical energy taking into account strain gradient elasticity and can be expressed as

$$\Psi^{\mathrm{Mech}}(\boldsymbol{\mathcal{E}}, \boldsymbol{\mathcal{G}}) = \Psi^{\mathrm{Elast}}(\boldsymbol{\mathcal{E}}) + \frac{1}{2}\mathcal{G}_{IJK}\, h_{IJKLMN}\, \mathcal{G}_{LMN}, \tag{17}$$

where Ψ^{Elast} is the elasticity energy density for any hyperelastic model, e.g. Neo-Hookean, and $\mathbf{h}$ is a constant sixth-order stain gradient elasticity tensor. The second term of (16) denotes the dielectric energy density. For a linear isotropic dielectric solid, its energy density per unit current volume can be defined as $\psi^{\mathrm{Diele}} = \frac{1}{2(\epsilon-\epsilon_0)} p_i p_i$ [19], transforming into Lagrangian frame resulting in the energy density per unit reference volume using (12)

$$\Psi^{\mathrm{Diele}}(\boldsymbol{\mathcal{E}}, \boldsymbol{P}) = \frac{1}{2J(\epsilon - \epsilon_0)} P_I\, C_{IJ}\, P_J, \tag{18}$$

where ϵ is the dielectric constant of the material. The last two terms of (12) represent the electro-mechanical coupling due to flexoelectric and piezoelectric effect. Inspired by [23], we postulate the following coupling:

$$\Psi^{\text{Flexo}}(\mathcal{G},\boldsymbol{P}) = -P_L\, f_{LIJK}\, \mathcal{G}_{IJK}, \tag{19}$$

$$\Psi^{\text{Piezo}}(\mathcal{E},\boldsymbol{P}) = -P_L\, \kappa_{LIJ}\, \mathcal{E}_{IJ}, \tag{20}$$

where f_{LIJK} and κ_{LIJ} are purely Lagrangian tensors and can be treated as material constants in this case. For dielectrics with centro-symmetric crystal structures, $\boldsymbol{\kappa}$ becomes a zero tensor.

To facilitate numerical computation, it is often useful to transfer the independent variable $\boldsymbol{P}$ into $\boldsymbol{E}$, and this can be done via the partial Legendre transformation, assuming one-to-one mapping [27], by defining the following dual internal potential

$$\bar{\Psi}^{\text{Int}}(\mathcal{E},\mathcal{G},\boldsymbol{E}) = \min_{\boldsymbol{P}} \left(\Psi^{\text{Int}}(\mathcal{E},\mathcal{G},\boldsymbol{P}) - \boldsymbol{P}\cdot\boldsymbol{E} \right). \tag{21}$$

The relation between independent variables $\boldsymbol{P}$ and $\boldsymbol{E}$ can be set through the stationary condition of (21) as $\boldsymbol{E}(\mathcal{E},\mathcal{G},\boldsymbol{P}) = \partial\Psi^{\text{Int}}/\partial\boldsymbol{P}$, which can be expanded explicitly as

$$E_L = \frac{\partial \Psi^{\text{Int}}}{\partial P_L} = \frac{1}{J(\epsilon-\epsilon_0)} C_{LM}\, P_M - f_{LIJK}\mathcal{G}_{IJK} - \kappa_{LIJ}\,\mathcal{E}_{IJ}. \tag{22}$$

The explicit expression of $\boldsymbol{P}$ can be inversely deduced from (22) as

$$P_L = J(\epsilon-\epsilon_0) C^{-1}_{LM}(E_M + f_{MIJK}\,\mathcal{G}_{IJK} + \kappa_{MIJ}\,\mathcal{E}_{IJ}). \tag{23}$$

Substituting (23) into (16), and defining $\boldsymbol{\mu} = (\epsilon-\epsilon_0)\,\boldsymbol{f}$ as the flexoelectric tensor, $\boldsymbol{\eta} = (\epsilon-\epsilon_0)\,\boldsymbol{\kappa}$ as the piezoelectric tensor, rearranging terms to obtain the dual internal potential as

$$\bar{\Psi}^{\text{Int}}(\mathcal{E},\mathcal{G},\boldsymbol{E}) = \bar{\Psi}^{\text{Mech}}(\mathcal{E},\mathcal{G}) + \bar{\Psi}^{\text{Diele}}(\mathcal{E},\boldsymbol{E}) + \bar{\Psi}^{\text{Flexo}}(\mathcal{E},\mathcal{G},\boldsymbol{E}) + \bar{\Psi}^{\text{Piezo}}(\mathcal{E},\boldsymbol{E}), \quad \text{in } \mathcal{B}_0, \tag{24}$$

where

$$\begin{aligned}
\bar{\Psi}^{\text{Mech}}(\mathcal{E},\mathcal{G}) &= \Psi^{\text{Elast}}(\mathcal{E}) + \frac{1}{2}\mathcal{G}_{IJK}\, h_{IJKLMN}\, \mathcal{G}_{LMN} - \frac{J}{2(\epsilon-\epsilon_0)}\mu_{IABK}\,\mathcal{G}_{ABK}\, C^{-1}_{IJ}\,\mu_{JABK}\,\mathcal{G}_{ABK} \\
&\quad - \frac{J}{2(\epsilon-\epsilon_0)}\eta_{IAB}\,\mathcal{E}_{AB}\, C^{-1}_{IJ}\,\eta_{JAB}\,\mathcal{E}_{AB} - \frac{J}{(\epsilon-\epsilon_0)}\mu_{IABK}\,\mathcal{G}_{ABK}\, C^{-1}_{IJ}\,\eta_{JAB}\,\mathcal{E}_{AB}, \\
\bar{\Psi}^{\text{Diele}}(\mathcal{E},\boldsymbol{E}) &= -\frac{J}{2}(\epsilon-\epsilon_0) E_I\, C^{-1}_{IJ}\, E_J, \\
\bar{\Psi}^{\text{Flexo}}(\mathcal{E},\mathcal{G},\boldsymbol{E}) &= -J\, E_I\, C^{-1}_{IJ}\,\mu_{JABK}\,\mathcal{G}_{ABK}, \\
\bar{\Psi}^{\text{Piezo}}(\mathcal{E},\boldsymbol{E}) &= -J\, E_I\, C^{-1}_{IJ}\,\eta_{JAB}\,\mathcal{E}_{AB}.
\end{aligned} \tag{25}$$

In the final step, the electrostatic field energy in the whole space, i.e. $\mathcal{B}\cup\mathcal{B}'$, should be taken into account to form the commonly used electric Gibbs free energy density. The electrostatic field energy density per unit current volume is $\psi^{\text{Elec}} = \frac{1}{2}\epsilon_0 e_i\, e_i$ [19], transforming into Lagrangian frame as energy density per unit reference volume as [31,59]

$$\bar{\Psi}^{\text{Elec}}(\mathcal{E},\boldsymbol{E}) = \frac{J\epsilon_0}{2} E_I\, C^{-1}_{IJ}\, E_J, \quad \text{in } \mathcal{B}_0\cup\mathcal{B}'_0. \tag{26}$$

Therefore, the electric Gibbs free energy density can be readily formed as

$$\bar{\Psi}^{\text{Gib}}(\mathcal{E},\mathcal{G},\boldsymbol{E}) = \bar{\Psi}^{\text{Int}}(\mathcal{E},\mathcal{G},\boldsymbol{E}) - \bar{\Psi}^{\text{Elec}}(\mathcal{E},\boldsymbol{E}), \quad \text{in } \mathcal{B}_0. \tag{27}$$

2.3. Strong form governing equations through variational principle

In this section, to maintain a focus on flexoelectricity and ensure conciseness, the piezoelectric effect is not included; that is, we set $\boldsymbol{\kappa} = \boldsymbol{0}$. However, the piezoelectric effect will be incorporated in the weak form formulations and numerical implementation for the verification case, as will be detailed in Sec. 4. Building upon the derivation from the previous section, the total energy functional governing the dielectric system (both the solid and the surrounding free space) can be expressed as follows.

$$\begin{aligned}
\Pi[\chi,\Phi] &= \int_{\mathcal{B}_0} \left(\bar{\Psi}^{\text{Gib}}(\mathcal{E},\mathcal{G},\boldsymbol{E}) - B_i\,\chi_i + Q\Phi \right) \mathrm{d}V - \int_{\mathcal{B}'_0} \bar{\Psi}^{\text{Elec}}(\mathcal{E},\boldsymbol{E})\,\mathrm{d}V \\
&\quad - \int_{\partial\mathcal{B}^T_0} \bar{T}_i\,\chi_i\,\mathrm{d}\Gamma - \int_{\partial\mathcal{B}^R_0} \bar{R}_i\, D^{(n)}\chi_i\,\mathrm{d}\Gamma - \int_{\partial\mathcal{B}^W_0} \bar{W}\,\Phi\,\mathrm{d}\Gamma \\
&= \int_{\mathcal{B}_0} \left(\Psi^{\text{Elast}} + \frac{1}{2}\mathcal{G}_{IJK}\,\bar{h}_{IJKLMN}\,\mathcal{G}_{LMN} - \frac{J\epsilon}{2} E_I\, C^{-1}_{IJ} E_J - J\, E_I\, C^{-1}_{IJ}\,\mu_{JABK}\,\mathcal{G}_{ABK} - B_i\,\chi_i + Q\Phi \right) \mathrm{d}V \\
&\quad + \int_{\mathcal{B}'_0} \left(-\frac{J\epsilon_0}{2} E_I\, C^{-1}_{IJ}\, E_J \right) \mathrm{d}V - \int_{\partial\mathcal{B}^T_0} \bar{T}_i\,\chi_i\,\mathrm{d}\Gamma - \int_{\partial\mathcal{B}^R_0} \bar{R}_i\, D^{(n)}\chi_i\,\mathrm{d}\Gamma - \int_{\partial\mathcal{B}^W_0} \bar{W}\,\Phi\,\mathrm{d}\Gamma,
\end{aligned} \tag{28}$$

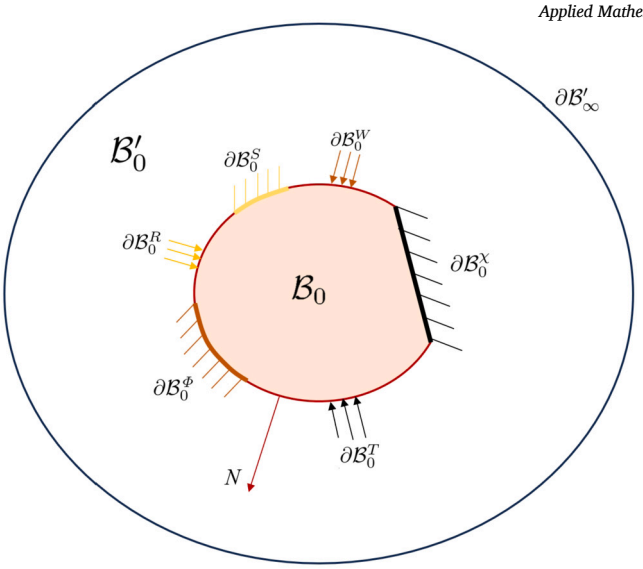

Fig. 2. Domain definition of the dielectric solid $\mathcal{B}_0$ immersed in free space $\mathcal{B}'_0$.

where the boundary of the reference body is split into disjoint Dirichlet and Neumann sets in view of different aspects such as $\partial\mathcal{B}_0 = \partial\mathcal{B}_0^\chi \cup \partial\mathcal{B}_0^T = \partial\mathcal{B}_0^S \cup \partial\mathcal{B}_0^R = \partial\mathcal{B}_0^\Phi \cup \partial\mathcal{B}_0^W$. The deformation map $\boldsymbol{\chi}$, normal derivatives of the deformation map $D^{(n)}\boldsymbol{\chi}$ and the electric potential $\boldsymbol{\Phi}$ are prescribed on the corresponding Dirichlet boundaries $\partial\mathcal{B}_0^\chi$, $\partial\mathcal{B}_0^S \cup$ and $\partial\mathcal{B}_0^\Phi$. The surface traction $\bar{\boldsymbol{T}}$, surface double traction $\bar{\boldsymbol{R}}$ and surface charge $\bar{W}$ are prescribed on the corresponding Neumann boundaries $\partial\mathcal{B}_0^T$, $\partial\mathcal{B}_0^R$ and $\partial\mathcal{B}_0^W$. The body force and free body charge densities are represented by $\boldsymbol{B}$ and Q, respectively. The domain definition is illustrated in Fig. 2. Note that for simplicity, the Dirichlet and Neumann boundary conditions for non-smooth regions of $\partial\mathcal{B}_0$ are not discussed in this paper, as compared with [23]. However, these conditions can be straightforwardly incorporated as necessary.

To recover the strong form governing equations from (28), its variation $\delta\Pi$ should vanish with respect to $\delta\boldsymbol{\chi}$ and $\delta\boldsymbol{\Phi}$, such that

$$\begin{aligned} &\delta\Pi(\boldsymbol{\chi},\boldsymbol{\Phi};\delta\boldsymbol{\chi}) = 0, \\ &\delta\Pi(\boldsymbol{\chi},\boldsymbol{\Phi};\delta\boldsymbol{\Phi}) = 0. \end{aligned} \tag{29}$$

The following variations can be derived through mathematical manipulations as

$$\begin{aligned} &\delta F_{iI}(\boldsymbol{\chi};\delta\boldsymbol{\chi}) := \delta\chi_{i,I}, \quad \delta\mathcal{F}_{iIJ}(\boldsymbol{\chi};\delta\boldsymbol{\chi}) := \delta\chi_{i,IJ}, \quad \delta\mathcal{E}_{IJ}(\boldsymbol{\chi};\delta\boldsymbol{\chi}) := \underset{IJ}{\operatorname{symm}}(\chi_{k,J}\,\delta\chi_{k,I}), \\ &\delta\mathcal{G}_{IJK}(\boldsymbol{\chi};\delta\boldsymbol{\chi}) := \underset{IJ}{\operatorname{symm}}(\chi_{k,J}\,\delta\chi_{k,IK} + \chi_{k,IK}\,\delta\chi_{k,J}), \quad \delta J(\boldsymbol{\chi};\delta\boldsymbol{\chi}) := J\,\delta\chi_{i,i}, \\ &\delta C_{IJ}^{-1}(\boldsymbol{\chi};\delta\boldsymbol{\chi}) := -(F_{Il}^{-1}F_{Jk}^{-1} + F_{Ik}^{-1}F_{Jl}^{-1})\,\delta\chi_{l,k} = -(X_{I,l}X_{J,k} + X_{I,k}X_{J,l})\,\delta\chi_{l,k}, \\ &\delta F_{Ik}^{-1}(\boldsymbol{\chi};\delta\boldsymbol{\chi}) := -F_{Il}^{-1}\,\delta\chi_{l,k} = -X_{I,l}\,\delta\chi_{l,k}, \quad \delta E_L(\boldsymbol{\Phi};\delta\boldsymbol{\Phi}) := -\delta\Phi_{,L}. \end{aligned} \tag{30}$$

For the ease of notation, the second Piola-Kirchhoff stress $\mathbf{S}$, the second Piola-Kirchhoff double stress $\boldsymbol{\Sigma}$, and the electric displacement of the dielectric solid $\boldsymbol{D}$ and the surrounding free space $\boldsymbol{D}^{\text{Env}}$ are defined as follows

$$\begin{aligned} S_{IJ} &:= \frac{\partial\bar{\Psi}^{\text{Mech}}}{\partial\mathcal{E}_{IJ}} = \frac{\Psi^{\text{Elast}}}{\partial\mathcal{E}_{IJ}} && \text{in } \mathcal{B}_0, \\ \Sigma_{IJK} &:= \frac{\bar{\Psi}^{\text{Gib}}}{\partial\mathcal{G}_{IJK}} = \bar{h}_{IJKLMN}\mathcal{G}_{LMN} - J E_M C_{ML}^{-1}\mu_{LIJK} && \text{in } \mathcal{B}_0, \\ D_L &:= -\frac{\partial\bar{\Psi}^{\text{Gib}}}{\partial E_L} = JC_{LK}^{-1}\left(\epsilon E_K + \mu_{KABC}\mathcal{G}_{ABC}\right) && \text{in } \mathcal{B}_0, \\ D_L^{\text{Env}} &:= -\frac{\partial\bar{\Psi}^{\text{Elec}}}{\partial E_L} = \epsilon_0 JC_{LK}^{-1}E_K && \text{in } \mathcal{B}'_0. \end{aligned} \tag{31}$$

Note that in the formulation of $\bar{\Psi}^{\text{Mech}}(\boldsymbol{\mathcal{E}},\boldsymbol{\mathcal{G}})$ in (25), the second term and the third term have the same structure and thus can be combined and simplified by a new material constant $\bar{h}_{IJKLMN}$ as:

$$\bar{h}_{IJKLMN} = h_{IJKLMN} - \frac{J}{(\epsilon-\epsilon_0)}\mu_{AIJK}C_{AB}^{-1}\mu_{BLMN}. \tag{32}$$

The additional stability requirement for $\bar{\boldsymbol{h}}$ is that it has to be semidefinite positive [23].

2.3.1. Mechanical governing equations

The variation of the total energy functional with respect to the deformation map can be written as

$$\begin{aligned}\delta\Pi(\chi,\boldsymbol{\Phi};\delta\chi) = &\int_{\mathcal{B}_0}\left(\delta\bar{\Psi}^{\mathrm{Gib}}(\boldsymbol{\mathcal{E}},\boldsymbol{\mathcal{G}},\boldsymbol{E};\delta\chi) - B_i\,\delta\chi_i\right)\mathrm{d}V - \int_{\mathcal{B}_0'}\delta\bar{\Psi}^{\mathrm{Elec}}(\boldsymbol{\mathcal{E}},\boldsymbol{E};\delta\chi)\,\mathrm{d}V\\ &- \int_{\partial\mathcal{B}_0^T}\bar{T}_i\,\delta\chi_i\,\mathrm{d}\Gamma - \int_{\partial\mathcal{B}_0^R}\bar{R}_i\,D^{(n)}\delta\chi_i\,\mathrm{d}\Gamma.\end{aligned} \tag{33}$$

To proceed, we first reformulate the first integral in (33) by applying the divergence theorem followed by integration by parts. For notational convenience, we also define an intermediate term $\widehat{D}_M := J\epsilon E_M + 2J\mu_{MABK}\mathcal{G}_{ABK}$. After substituting (30), the first integral of (33) can be expressed as

$$\begin{aligned}&\int_{\mathcal{B}_0}\delta\bar{\Psi}^{\mathrm{Gib}}(\boldsymbol{\mathcal{E}},\boldsymbol{\mathcal{G}},\boldsymbol{E};\delta\chi)\,\mathrm{d}V\\
&= \int_{\mathcal{B}_0}\left\{S_{IJ}\,\delta\mathcal{E}_{IJ}(\chi;\delta\chi) + \Sigma_{IJK}\,\delta\mathcal{G}_{IJK}(\chi;\delta\chi) - \frac{1}{2}E_I\widehat{D}_J\,\delta C^{-1}_{IJ}(\chi;\delta\chi) - \frac{1}{2J}E_I C^{-1}_{IJ}\widehat{D}_J\,\delta J(\chi;\delta\chi)\right\}\mathrm{d}V\\
&= \int_{\mathcal{B}_0}\frac{1}{2}\Big\{\nabla_J\cdot(S_{IJ}\,\chi_{k,I}\,\delta\chi_k) - (S_{IJ}\,\chi_{k,I})_{,J}\,\delta\chi_k + \nabla_I\cdot(S_{IJ}\,\chi_{k,J}\,\delta\chi_k) - (S_{IJ}\,\chi_{k,J})_{,I}\,\delta\chi_k\\
&+ \nabla_K\cdot(\Sigma_{IJK}\,\chi_{k,I}\,\delta\chi_{k,J}) - \nabla_J\cdot\left[(\Sigma_{IJK}\,\chi_{k,I})_{,K}\,\delta\chi_k\right] + (\Sigma_{IJK}\,\chi_{k,I})_{,KJ}\,\delta\chi_k\\
&+ \nabla_K\cdot(\Sigma_{IJK}\,\chi_{k,J}\,\delta\chi_{k,I}) - \nabla_I\cdot\left[(\Sigma_{IJK}\,\chi_{k,J})_{,K}\,\delta\chi_k\right] + (\Sigma_{IJK}\,\chi_{k,J})_{,KI}\,\delta\chi_k\\
&+ \nabla_I\cdot(\Sigma_{IJK}\,\chi_{k,JK}\,\delta\chi_k) - (\Sigma_{IJK}\,\chi_{k,JK})_{,I}\,\delta\chi_k + \nabla_J\cdot(\Sigma_{IJK}\,\chi_{k,IK}\,\delta\chi_k) - (\Sigma_{IJK}\,\chi_{k,IK})_{,J}\,\delta\chi_k\\
&+ \nabla_I\cdot\left[(E_L C^{-1}_{LI}C^{-1}_{JM}\widehat{D}_M - \frac{1}{2}E_L C^{-1}_{LM}\widehat{D}_M C^{-1}_{IJ})\,\chi_{k,J}\,\delta\chi_k\right] - \left[(E_L C^{-1}_{LI}C^{-1}_{JM}\widehat{D}_M - \frac{1}{2}E_L C^{-1}_{LM}\widehat{D}_M C^{-1}_{IJ})\,\chi_{k,J}\right]_{,I}\delta\chi_k\\
&+ \nabla_J\cdot\left[(E_L C^{-1}_{LI}C^{-1}_{JM}\widehat{D}_M - \frac{1}{2}E_L C^{-1}_{LM}\widehat{D}_M C^{-1}_{IJ})\,\chi_{k,I}\,\delta\chi_k\right] - \left[(E_L C^{-1}_{LI}C^{-1}_{JM}\widehat{D}_M - \frac{1}{2}E_L C^{-1}_{LM}\widehat{D}_M C^{-1}_{IJ})\,\chi_{k,I}\right]_{,J}\delta\chi_k\Big\}\mathrm{d}V\\
&= \int_{\partial\mathcal{B}_0}\frac{1}{2}\left[(S_{IJ} - \Sigma_{IJK,K} + S^{\mathrm{MW}}_{IJ})\,\chi_{k,I}N_J\right]\delta\chi_k\,\mathrm{d}\Gamma + \int_{\partial\mathcal{B}_0}\frac{1}{2}\left[(S_{IJ} - \Sigma_{IJK,K} + S^{\mathrm{MW}}_{IJ})\,\chi_{k,J}N_I\right]\delta\chi_k\,\mathrm{d}\Gamma\\
&- \int_{\mathcal{B}_0}\frac{1}{2}\left[(S_{IJ} - \Sigma_{IJK,K} + S^{\mathrm{MW}}_{IJ})\,\chi_{k,I}\right]_{,J}\delta\chi_k\,\mathrm{d}V - \int_{\mathcal{B}_0}\frac{1}{2}\left[(S_{IJ} - \Sigma_{IJK,K} + S^{\mathrm{MW}}_{IJ})\,\chi_{k,J}\right]_{,I}\delta\chi_k\,\mathrm{d}V\\
&+ \int_{\partial\mathcal{B}_0}\frac{1}{2}\left(\Sigma_{IJK}\,\chi_{k,I}\,\delta\chi_{k,J} + \Sigma_{IJK}\,\chi_{k,J}\,\delta\chi_{k,I}\right)N_K\,\mathrm{d}\Gamma.\end{aligned} \tag{34}$$

In the last equation of (34), $\mathbf{S}^{\mathrm{MW}}$ is the second Piola-Maxwell stress tensor induced by polarization under external electric field and electromechanical coupling, and it is defined as

$$\begin{aligned}S^{\mathrm{MW}}_{IJ} &:= E_L C^{-1}_{LI}C^{-1}_{JM}\widehat{D}_M - \frac{1}{2}E_L C^{-1}_{LM}\widehat{D}_M C^{-1}_{IJ},\\ &= E_L C^{-1}_{LI}\widetilde{D}_J - \frac{1}{2}E_L\widetilde{D}_L C^{-1}_{IJ}.\end{aligned} \tag{35}$$

Note that in (35) $\widetilde{D}_L = C^{-1}_{LM}\widehat{D}_M$ is the auxiliary electric displacement formed by applying an inverse deformation mapping to $\widehat{D}_M$, which carries a more clear physical meaning. The Eulerian counterpart of $\mathbf{S}^{\mathrm{MW}}$ can be forwardly obtained, using (6) and (10), as

$$\boldsymbol{\sigma}^{\mathrm{MW}} := \boldsymbol{e}\otimes\widetilde{\boldsymbol{d}} - \frac{1}{2}(\boldsymbol{e}\cdot\widetilde{\boldsymbol{d}})\mathbf{I}, \tag{36}$$

where $\widetilde{d}_l := \frac{1}{J}F_{lL}\widetilde{D}_L$ is the Eulerian counterpart of $\widetilde{D}_L$.[1] We would like to note that (35) and (36) satisfy Minkovski's formulation in Table 1 and apply to a broad range of materials, extending and complementing the current body of research on Maxwell stress.

Remark 1. The auxiliary electric displacement apparently has the following relation with the actual electric displacement defined in (31): $\widetilde{D}_L = D_L + JC^{-1}_{LM}\mu_{MABK}\mathcal{G}_{ABK}$. The reason for this additional term lies in that, when defining D_L by differentiating the free energy with respect to E_L, symmetric quadratic contributions involving electric field is evenly "split". In contrast, when deriving the Maxwell stress, these same terms are not symmetrically partitioned and an additional term appears. This discrepancy does not imply

[1] The complete expression is $\widetilde{d}_l = \epsilon e_l + 2\mu_{MABK}F^{-1}_{Ml}(F_{aAK}F_{bB}\epsilon_{ab} + F_{aA}F_{bBK}\epsilon_{ab} + F_{aA}F_{bB}F_{kK}g_{abk})$.

any new physical effect; it simply reflects that the symmetrical reduction inherent in the definition of D_L does not occur when the variation is taken with respect to mechanical quantities.

The last integral in the last equation of (34) can be calculated by splitting the variation $\delta\chi_{k,J}$ into tangential and normal gradient components as

$$\begin{aligned}\delta\chi_{k,J} &= D_J^{(t)}\delta\chi_k + N_J D^{(n)}\delta\chi_k,\\ D_J^{(t)} &\equiv (\delta_{JK} - N_J N_K)\partial_K,\\ D^{(n)} &\equiv N_K\partial_K,\end{aligned} \tag{37}$$

so that it can be simplified into

$$\int_{\partial\mathcal{B}_0} \frac{1}{2}\left(\Sigma_{IJK}\,\chi_{k,I}\,\delta\chi_{k,J} + \Sigma_{IJK}\,\chi_{k,J}\,\delta\chi_{k,I}\right)N_K\,\mathrm{d}\Gamma = \int_{\partial\mathcal{B}_0}\widetilde{T}_k^{(t)}\,\delta\chi_k\,\mathrm{d}\Gamma + \int_{\partial\mathcal{B}_0}\widetilde{T}_k^{(n)}D^{(n)}\delta\chi_k\,\mathrm{d}\Gamma, \tag{38}$$

where

$$\begin{aligned}\widetilde{T}_k^{(t)} &= \frac{1}{2}\big[\Sigma_{IJK}N_K(N_J\,\chi_{k,I} + N_I\,\chi_{k,J})D_L^{(t)}N_L - N_K(\chi_{k,I}D_J^{(t)}\Sigma_{IJK} + \chi_{k,J}D_I^{(t)}\Sigma_{IJK})\\ &\qquad - \Sigma_{IJK}(\chi_{k,I}D_J^{(t)}N_K + \chi_{k,J}D_I^{(t)}N_K)\big],\\ \widetilde{T}_k^{(n)} &= \frac{1}{2}\Sigma_{IJK}N_K\left(\chi_{k,I}N_J + \chi_{k,J}N_I\right).\end{aligned} \tag{39}$$

Detailed derivations can be found in Appendix A.

In a similar approach, the second integral of (33) can be derived as

$$\int_{\mathcal{B}_0'} -\delta\bar{\Psi}^{\mathrm{Elec}}(\boldsymbol{\mathcal{E}},\boldsymbol{E};\delta\chi)\,\mathrm{d}V = \int_{\partial\mathcal{B}_0'} S_{IJ}^{\mathrm{MWE}}\,\chi_{k,I}N_J'\,\delta\chi_k\,\mathrm{d}\Gamma + \int_{\partial\mathcal{B}_\infty'} S_{IJ}^{\mathrm{MWE}}\,\chi_{k,I}N_J'\,\delta\chi_k\,\mathrm{d}\Gamma - \int_{\mathcal{B}_0'}(S_{IJ}^{\mathrm{MWE}}\,\chi_{k,I})_{,J}\,\delta\chi_k\,\mathrm{d}V, \tag{40}$$

where the second Piola-Maxwell stress in the surrounding free space $\mathbf{S}^{\mathrm{MWE}}$ is defined as

$$S_{IJ}^{\mathrm{MWE}} := J\epsilon_0 E_L C_{LI}^{-1}C_{JM}^{-1}E_M - \frac{1}{2}J\epsilon_0 E_L C_{LM}^{-1}E_M C_{IJ}^{-1}. \tag{41}$$

The Eulerian counterpart of S_{IJ}^{MWE} can thus be obtained as

$$\boldsymbol{\sigma}^{\mathrm{MWE}} := \epsilon_0\,\boldsymbol{e}\otimes\boldsymbol{e} - \frac{1}{2}\epsilon_0(\boldsymbol{e}\cdot\boldsymbol{e})\mathbf{I}. \tag{42}$$

On use of $E_L = -\nabla_L\Phi$ and Φ must satisfy (13) in $\mathcal{B}'$, it can be assumed that $\Phi \sim 1/|\mathbf{x}|$ as $|\mathbf{x}|\to\infty$, so that $E_L \sim 1/|\mathbf{x}^2|$ as $|\mathbf{x}|\to\infty$ and thus the second integral in (40) vanishes [31]. It is immediately evident that $\mathbf{S}^{\mathrm{MWE}}$ is symmetric, as there is no polarization in the free space, and thus $\boldsymbol{d}^{\mathrm{Env}} = \epsilon_0\boldsymbol{e}$. However, in the dielectric solid $\mathbf{S}^{\mathrm{MW}}$ may not be symmetric. Nonetheless, the rotational balance of the dielectric solid mandates that the total stress $\mathbf{S}^{\mathrm{tot}} := \mathbf{S} - \nabla\boldsymbol{\Sigma} + \mathbf{S}^{\mathrm{MW}}$ must be symmetric [60]. Therefore, the terms with alternating indices in the last equation of (34) can be combined and thus simplified. Collecting all parts, (33) can be reformulated as

$$\begin{aligned}\delta\Pi(\chi,\Phi;\delta\chi) = &\int_{\partial\mathcal{B}_0^T}\left[(S_{IJ} - \Sigma_{IJK,K} + S_{IJ}^{\mathrm{MW}} - S_{IJ}^{\mathrm{MWE}})\,\chi_{k,I}N_J + \widetilde{T}_k^{(t)} - \bar{T}_k\right]\delta\chi_k\,\mathrm{d}\Gamma\\ &- \int_{\mathcal{B}_0}\left[\left((S_{IJ} - \Sigma_{IJK,K} + S_{IJ}^{\mathrm{MW}})\,\chi_{k,I}\right)_{,J} + B_k\right]\delta\chi_k\,\mathrm{d}V - \int_{\mathcal{B}_0'}(S_{IJ}^{\mathrm{MWE}}\,\chi_{k,I})_{,J}\,\delta\chi_k\,\mathrm{d}V\\ &+ \int_{\partial\mathcal{B}_0^R}(\widetilde{T}_k^{(n)} - \bar{R}_k)D^{(n)}\delta\chi_k\,\mathrm{d}\Gamma,\end{aligned} \tag{43}$$

where $\boldsymbol{N}' = -\boldsymbol{N}$ on $\partial\mathcal{B}_0$ has been applied in the first integral. The mechanical governing equations can be obtained by satisfying the stationary conditions (29) as

$$\begin{cases}\left((S_{IJ} - \Sigma_{IJK,K} + S_{IJ}^{\mathrm{MW}})\,\chi_{k,I}\right)_{,J} + B_k = 0 & \text{in } \mathcal{B}_0,\\ (S_{IJ} - \Sigma_{IJK,K} + S_{IJ}^{\mathrm{MW}} - S_{IJ}^{\mathrm{MWE}})\,\chi_{k,I}N_J + \widetilde{T}_k^{(t)} = \bar{T}_k & \text{on } \partial\mathcal{B}_0^T,\\ (S_{IJ}^{\mathrm{MWE}}\,\chi_{k,I})_{,J} = 0 & \text{in } \mathcal{B}_0',\\ \widetilde{T}_k^{(n)} = \bar{R}_k & \text{on } \partial\mathcal{B}_0^R.\end{cases} \tag{44}$$

2.3.2. Electric governing equations

The variation of the total energy functional with respect to the electric potential can be written as

$$\begin{aligned}\delta\Pi(\chi,\Phi;\delta\Phi) &= \int_{\mathcal{B}_0}\left(\delta\bar{\Psi}^{\mathrm{Gib}}(\mathcal{E},\mathcal{G},\boldsymbol{E};\delta\Phi)+Q\,\delta\Phi\right)\mathrm{d}V-\int_{\mathcal{B}_0'}\delta\bar{\Psi}^{\mathrm{Elec}}(\mathcal{E},\boldsymbol{E};\delta\Phi)\,\mathrm{d}V-\int_{\partial\mathcal{B}_0^W}\bar{W}\,\delta\Phi\,\mathrm{d}\Gamma\\ &= \int_{\mathcal{B}_0}\left(-D_L\,\delta E_L+Q\,\delta\Phi\right)\mathrm{d}V+\int_{\mathcal{B}_0'}\left(-D_L^{\mathrm{Env}}\,\delta E_L\right)\mathrm{d}V-\int_{\partial\mathcal{B}_0^W}\bar{W}\,\delta\Phi\,\mathrm{d}\Gamma\\ &= \int_{\partial\mathcal{B}_0^W}\left(D_L N_L-D_L^{\mathrm{Env}}N_L-\bar{W}\right)\delta\Phi\,\mathrm{d}\Gamma-\int_{\mathcal{B}_0}\left(D_{L,L}-Q\right)\delta\Phi\,\mathrm{d}V-\int_{\mathcal{B}_0'}D_{L,L}^{\mathrm{Env}}\delta\Phi\,\mathrm{d}V+\int_{\partial\mathcal{B}_\infty'}D_L^{\mathrm{Env}}N_L'\,\mathrm{d}\Gamma,\end{aligned}\tag{45}$$

where the last integral over $\partial\mathcal{B}_\infty'$ vanishes due to the same reason mentioned in the last section. The electric governing equations can thus be obtained by (29) as

$$\begin{cases}D_{L,L}=Q & \text{in } \mathcal{B}_0,\\ \left(D_L-D_L^{\mathrm{Env}}\right)N_L=\bar{W} & \text{on } \partial\mathcal{B}_0^W,\\ D_{L,L}^{\mathrm{Env}}=0 & \text{in } \mathcal{B}_0'.\end{cases}\tag{46}$$

Therefore, (44) and (46) form the complete strong form governing equations for the dielectric system.

3. Consistent linearization and numerical implementation

In this section, a numerical approach is developed to solve the boundary value problem as defined by the strong form governing equations (44) and (46). Isogeometric analysis (IGA) framework is employed to model the higher order continuity required by the smoothness of strain gradient in the dielectric solid. For this purpose, a degree $p=3$ is utilized. Given the involvement of electromechanical coupling and finite deformation, the problem inherently becomes highly nonlinear. This complexity necessitates the linearization of the residual term, enabling the application of the Newton-Raphson algorithm for iterative solution searching. For implementation the code is developed based on an open-source MATLAB library NLIGA [61].

In light of (34), the weak form formulation for total energy functional with respect to both $\delta\chi$ and $\delta\Phi$ can be rewritten as

$$\begin{aligned}\delta\Pi(\chi,\Phi;\delta\chi,\delta\Phi) &= \int_{\mathcal{B}_0}\left((S_{IJ}+S_{IJ}^{\mathrm{MW}})\,\delta\mathcal{E}_{IJ}+\Sigma_{IJK}\,\delta\mathcal{G}_{IJK}-D_L\,\delta E_L+Q\,\delta\Phi-B_i\,\delta\chi_i\right)\mathrm{d}V\\ &+\int_{\mathcal{B}_0'}\left(S_{IJ}^{\mathrm{MWE}}\,\delta\mathcal{E}_{IJ}-D_L^{\mathrm{Env}}\,\delta E_L\right)\mathrm{d}V-\int_{\partial\mathcal{B}_0^T}\bar{T}_i\,\delta\chi_i\,\mathrm{d}\Gamma-\int_{\partial\mathcal{B}_0^R}\bar{R}_i\,D^{(n)}\delta\chi_i\,\mathrm{d}\Gamma-\int_{\partial\mathcal{B}_0^W}\bar{W}\,\delta\Phi\,\mathrm{d}\Gamma.\end{aligned}\tag{47}$$

Within each time step i, the residual of the discrete total energy functional can be defined as $\mathcal{R}_{es}(\chi^i,\Phi^i,\delta\chi,\delta\Phi)=\delta\Pi(\chi^i,\Phi^i;\delta\chi,\delta\Phi)$. The residual is then linearized for the construction of the tangent stiffness matrix. Subsequently, the Newton-Raphson method is employed to solve the resultant linear system and iteratively update the values of displacement and electric potential until they meet a predefined convergence criterion. The linearization process begins with the calculation of a truncated Taylor expansion of the residual as

$$\mathrm{Lin}\,\mathcal{R}_{es}(\chi^i,\Phi^i,\delta\chi,\delta\Phi)=\mathcal{R}_{es}(\chi^i,\Phi^i,\delta\chi,\delta\Phi)+\frac{\partial\mathcal{R}_{es}(\chi,\Phi,\delta\chi,\delta\Phi)}{\partial\chi}\Big|^i\Delta\chi+\frac{\partial\mathcal{R}_{es}(\chi,\Phi,\delta\chi,\delta\Phi)}{\partial\Phi}\Big|^i\Delta\Phi.\tag{48}$$

The solution is sought by requiring the residual to vanish, yielding

$$\frac{\partial\mathcal{R}_{es}(\chi,\Phi,\delta\chi,\delta\Phi)}{\partial\chi}\Big|^i\Delta\chi+\frac{\partial\mathcal{R}_{es}(\chi,\Phi,\delta\chi,\delta\Phi)}{\partial\Phi}\Big|^i\Delta\Phi=-\mathcal{R}_{es}(\chi^i,\Phi^i,\delta\chi,\delta\Phi),\tag{49}$$

which can be rearranged into the following algebraic system of equations for increments $\{\Delta\chi,\Delta\Phi\}$ in matrix-vector notation:

$$\begin{bmatrix}\mathbf{K}_{\chi\chi} & \mathbf{K}_{\chi\Phi}\\ \mathbf{K}_{\Phi\chi} & \mathbf{K}_{\Phi\Phi}\end{bmatrix}\cdot\begin{bmatrix}\Delta\chi\\ \Delta\Phi\end{bmatrix}=-\begin{bmatrix}\mathcal{R}_\chi\\ \mathcal{R}_\Phi\end{bmatrix}.\tag{50}$$

Detailed derivation of the variation of the residual $\mathcal{R}_{es}$ can be found in Appendix B. After solving the linear system, the nodal displacements and electric potentials are updated until reaching the convergence criterion via

$$\begin{aligned}\chi^{i+1}&=\chi^i+\Delta\chi,\\ \Phi^{i+1}&=\Phi^i+\Delta\Phi.\end{aligned}\tag{51}$$

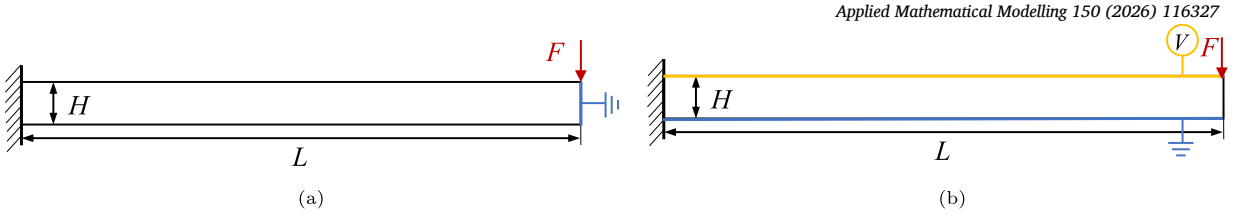

Fig. 3. Schematic of a cantilever beam with (a) open circuit setting and (b) closed circuit setting.

4. Numerical examples of linear flexoelectricity

This section presents a cantilever beam subjected to a tip load, which is a widely adopted benchmark case in the context of linear flexoelectricity, to verify the proposed nonlinear flexoelectric framework. For material characterization in both scenarios, we employ the Saint-Venant-Kirchhoff model, details of which can be found in Appendix C.

The cantilever beam model is the simplest model for the illustration of a nanogenerator. As shown in Fig. 3, the beam with dimensions $L \times H$ is fixed at the left-end and a tip load is applied to the top right-end. Two electrical boundary conditions, namely open and closed circuit settings, are studied. In the open circuit setting, the right end is grounded, i.e. zero electrical potential is applied. In the closed circuit setting, the top edge of the beam is grounded while an electrode is deposited on the bottom edge to prescribe an electric potential V. Due to the electromechanical coupling effect, the mechanical deformation can generate electric energy. The performance of the energy conversion can be evaluated by the electromechanical coupling factor, defined as

$$k_{\text{eff}}^2 := \frac{W_{\text{elec}}}{W_{\text{mech}}} = \frac{\int_{\mathcal{B}} \frac{1}{2}\, \epsilon \boldsymbol{E} \cdot \boldsymbol{E}\, \mathrm{d}V}{\int_{\mathcal{B}} \frac{1}{2}\, \boldsymbol{\sigma} : \boldsymbol{\varepsilon}\, \mathrm{d}V}, \tag{52}$$

where W_{elec} and W_{mech} represent electrical energy and mechanical energy, respectively. The normalized effective piezoelectric coefficient (NEPC) $\eta^\star$ can thus be defined as

$$\eta^\star := \frac{k_{\text{eff}}}{k_{\text{piezo}}}, \tag{53}$$

where k_{piezo} represents the electromechanical coupling factor for non-flexoelectric materials.

If the problem is restricted to 1D, i.e. only σ_{11} in stress $\boldsymbol{\sigma}$ and E_2 in electric field $\boldsymbol{E}$ are non-zero, the analytical solution of the electromechanical coupling factor has been derived (originally in [62] and corrected in [55]) as

$$k_{\text{eff}}^{\text{1D}} = \frac{\alpha}{1+\alpha}\sqrt{\frac{1}{\epsilon Y}\left(\eta_{\text{T}}^2 + 12\left(\frac{\mu_{\text{T}}}{H}\right)^2\right)}, \tag{54}$$

where $\alpha := \epsilon/\epsilon_0 - 1$ is the electric susceptibility, Y is the Young's modulus of the dielectric, η_{T} and μ_{T} are the transversal piezoelectric and transversal flexoelectric coefficient, respectively. In this case, the NEPC can be expressed analytically as

$$\eta_{\text{1D}}^\star = \frac{k_{\text{eff}}^{\text{1D}}}{k_{\text{piezo}}^{\text{1D}}} = \sqrt{1 + 12\left(\frac{\mu_{\text{T}}}{\eta_{\text{T}} H}\right)^2}. \tag{55}$$

A simplified model is numerically computed for comparison with the analytical solution. The material parameters for a single barium titanate ($BaTiO_3$) crystal are adopted from [45] and are listed as follows: $Y = 100$ GPa, Poisson's ratio $\nu = 0$, $\eta_{211} = \eta_{\text{T}} = -4.4\,\text{C/m}^2$, $\mu_{1221} = \mu_{2112} = \mu_{\text{T}} = 1\,\mu\text{C/m}$, $\epsilon = 12.48\,\text{nC/Vm}$, $\epsilon_0 = 8.854 \times 10^{-12}\,\text{C/Vm}$. The load data is $F = 100\,\mu\text{N}$. The beam thickness is normalized by $H_0 = -\mu_{\text{T}}/\eta_{\text{T}}$ and the beam length is set at $L = 20H$. The analytical and numerical results for this simplified 1D problem can be seen in Fig. 4 and an excellent agreement is observed. It is also observed that the electric performance of the beam enhances with decreasing thickness, attributable to the size-dependent nature of flexoelectricity. Conversely, as the beam thickness increases, the Normalized Electric Polarization Coefficient (NEPC) steadily decreases and converges to 1, indicating the diminishing significance of the flexoelectric effect in thicker beams.

A more realistic case study considering the 2D effect of the material has also been conducted. For this analysis, a Poisson's ratio $\nu = 0.37$ is employed. Besides the transversal flexoelectric effect, the longitudinal flexoelectric effect is incorporated, assigning $\mu_{1111} = \mu_{2222} = \mu_L = 1\,\mu\text{C/m}$. The remaining parameters are kept consistent with the 1D case. The results, presented in Fig. 4, indicate that while the trend of the Normalized Electric Polarization Coefficient (NEPC) with normalized beam thickness remains consistent, the magnitude of NEPC is notably lower compared with the 1D case. Specifically, at the reference thickness H_0, the NEPC is almost half of what it is in the 1D case. Additionally, NEPC values are evaluated under a closed circuit setting, keeping the same material parameters and allowing the electric potential of the bottom edge to be free. NEPC values in the closed circuit setting are slightly lower than those in the open circuit setting in 2D case, which aligns with findings reported in previous literature [45].

In the second case, which focuses on the closed circuit setting, we investigate a scenario of pure electric loading by setting $F = 0\,\text{N}$ and $V = -8H\,\text{MV}$. Under this electric loading, the beam undergoes deflection. This occurs because the flexoelectric effect couples the electric field with the strain gradient, causing the beam to bend similarly to an actuator, thereby generating a bending curvature.

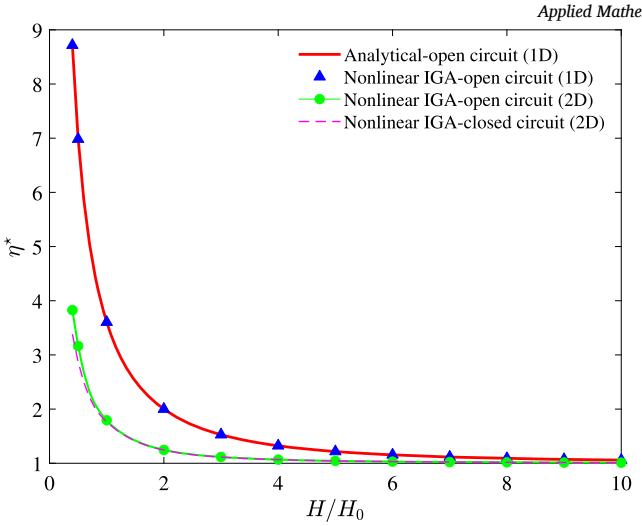

Fig. 4. (a) Normalized effective piezoelectric coefficient $\eta^\star$ with normalized beam thickness H/H_0.

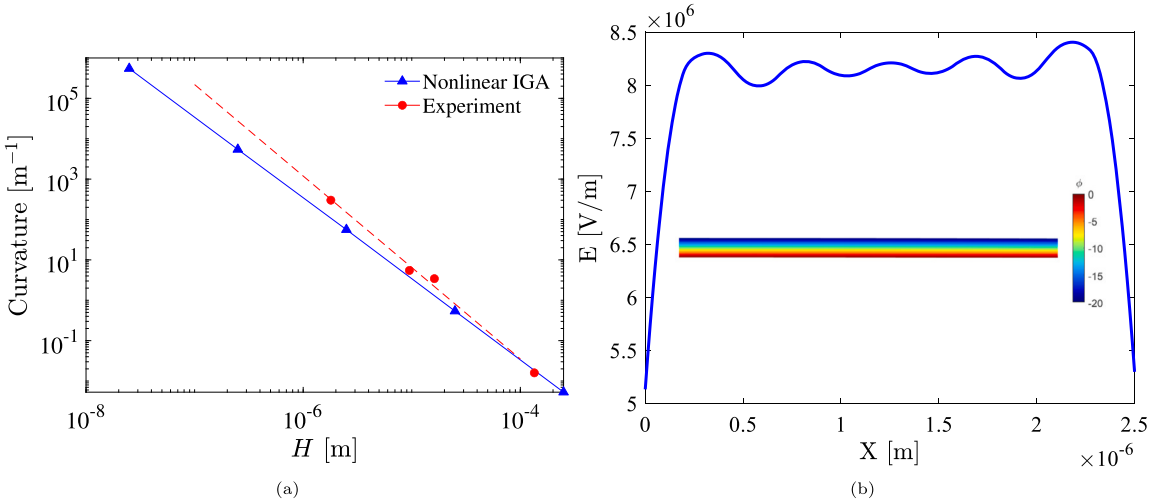

Fig. 5. Results of the closed circuit setting: (a) curvature of the beam with respect to the size; (b) electric field over the thickness of the cantilever beam.

The magnitude of the bending curvature is dependent on the size of the beam. As shown in Fig. 5(a), the results demonstrate good agreement with experimental findings reported in [63]. The distribution of the vertical electric field across the beam, as depicted in Fig. 5, reveals that the electric field remains approximately uniform throughout most of the beam's thickness, with an exception near the edges where a sudden drop occurs. This high electric field gradient, characterized by an opposite sign at the edges, induces significant local stress due to the converse flexoelectric effect, consequently generating a clockwise moment. These findings are consistent with the literature [45,55]. Notably, the nonlinear flexoelectric model exhibits more fluctuations in the electric field compared with its linear counterpart.

5. Numerical examples of nonlinear flexoelectricity undergoing finite deformation

This section showcases the capability of the proposed nonlinear flexoelectric model to simulate finite deformations in a cantilever beam. The deformations are induced either by mechanical loading in the open circuit setting or by electric loading in the closed circuit setting. The model setups are similar to those depicted in Fig. 3, with adjustments to the external load conditions. The same geometrical and material parameters are used for both cases: thickness $H = 1\,\mu\text{m}$, length $L = 20H$, Young's modulus $Y = 1\,\text{GPa}$, Poisson's ratio $\nu = 0.3$, dielectric constant $\epsilon = 0.092\,\text{nC/Vm}$ and characteristic length $l_s = 0$, corresponding to polyvinylidene fluoride (PVDF). The Neo-Hookean model, detailed in Appendix C, is utilized to characterize the properties of the hyperelastic material, including the mechanical stress term and the related tangent stiffness tensor. The flexoelectric coefficient tensor $\boldsymbol{\mu}$ includes three independent constants: the longitudinal coefficient μ_L (corresponding to components μ_{1111} and μ_{2222} in 2D case), the transversal coefficient μ_T (corresponding to μ_{1221} and μ_{2112}), and the shear coefficient μ_S (corresponding to $\mu_{1122}, \mu_{2211}, \mu_{1212}$ and μ_{2121}). In the

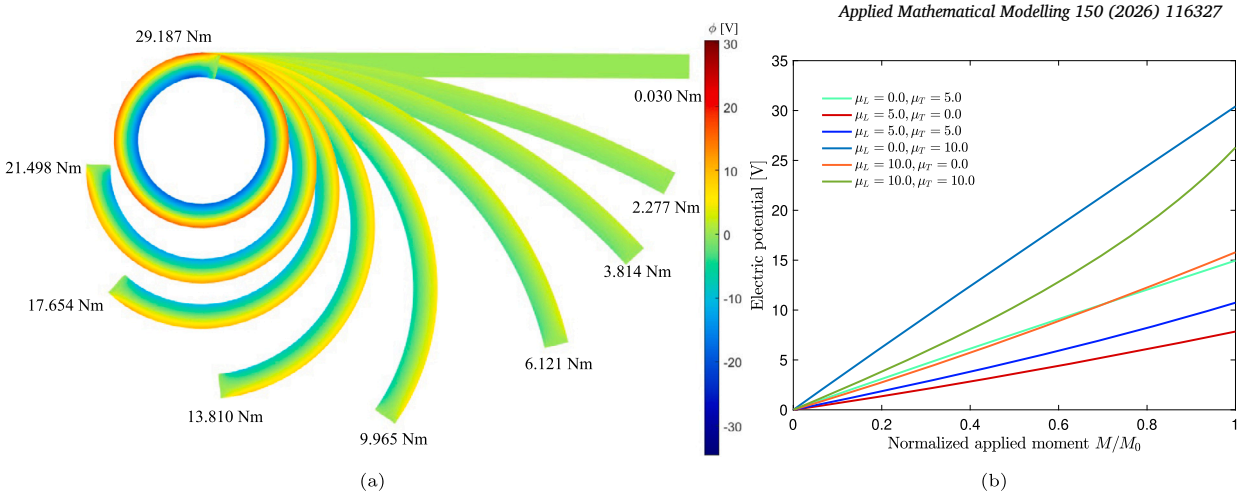

Fig. 6. (a) Screenshots on deformed configuration and electric distribution of the beam under incrementally applied moments with $\mu_L = 0$ and $\mu_T = 10\,\mathrm{nC/m}$. (b) Evolution of the maximum electric potential with normalized applied moment.

forthcoming simulations, the impact of μ_T and μ_L will be studied, whereas μ_S is assumed zero as its significance is comparatively negligible [23]. Electric breakdown concerns are also omitted, implying that the dielectric can withstand any electric field without turning conductive. A convergence rate criterion tolerance of 10^{-3} and a mesh size of $H/5$ are maintained in all simulations.

5.1. Finite deformation under mechanical loading

The first example involves finite deformation resulting from mechanical causes. Specifically, a moment (directed inwards, as per the paper's perspective) instead of a force is applied to the right end of the beam depicted in Fig. 3(a). Due to the flexoelectric coupling, an electric potential redistribution across the beam is expected. As the applied moment increases, the beam undergoes finite deformation and eventually rolls up to form a circle at a certain level of applied moment, as illustrated in Fig. 6(a). It is observed that after deformation, the top edge of the beam exhibits positive electric potentials, while negative potentials are attributed to the bottom edge. Furthermore, the absolute value of the electric potential escalates with the degree of deformation.

In light of such phenomenon, various combinations of μ_T and μ_L are explored to compare the maximum electric potential generated during deformation. The outcomes of these comparisons are presented in Fig. 6, where the x-axis is normalized by a moment $M_0 = 30\,\mathrm{Nm}$. These results highlight that μ_T plays a pivotal role in the electric performance, as the highest electric potential is achieved when μ_T alone is assigned a large value. It is also noted that when either μ_T or μ_L is used independently, the electric potential increases linearly with the applied moment. This near-linear behavior, despite the nonlinear material model, is attributed to the pure bending load, where the resulting strain gradients are approximately proportional to the applied moment over the deformation range studied. However, when both are used simultaneously, the relationship between electric potential and applied moment transitions into a nonlinear one, due to the more complex coupling terms in the energy functional.

5.2. Finite deformation under electric loading

In the previous example, the direct flexoelectric effect in the nonlinear regime was demonstrated. In this example, we focus on the converse effect, where the beam functions as an actuator under electric loading. As depicted in Fig. 3(b), a large electric potential is applied to the top edge of the beam under closed circuit conditions, while the tip load is removed. The applied electric potential induces a transversal electric field across the beam's thickness, resulting in a non-uniform strain field due to the flexoelectric effect, and elongation of the beam due to the Maxwell effect. Fig. 7 exhibits the axial elongations of the beam assigning various transversal flexoelectric coefficients. The numerical results obtained by our model agree well with the referenced first-order approximation derived in [23], especially for low applied electric potentials based on which the analytical results are obtained. Remarkably, the elongations tend to increase under large transversal flexoelectric coefficients, indicating perfectly the contribution of flexoelectricity to the Maxwell stress.

Upon the same electric loading, the bending curvature of the beam has been theoretically derived to be uniform [23]. Consequently, the beam can deform into a circular shape with sufficient electric loading, as demonstrated in Fig. 8(a). Numerically, the bending curvature is recorded at each incremental time step under various combinations of flexoelectric coefficients. This curvature is normalized by the curvature needed to form a closed circle, denoted as $\rho_0^{-1}(\boldsymbol{\Phi}) = 2\pi/\hat{L}(\boldsymbol{\Phi})$, where $\hat{L}(\boldsymbol{\Phi})$ represents the axial length of the beam after elongation. The results are presented in Fig. 8(b). It is observed that the transversal flexoelectric coefficient μ_T significantly influences the rate of curvature evolution. A negative longitudinal flexoelectric coefficient μ_L enhances this rate, while a positive μ_L diminishes it. If only a positive μ_L is applied to the flexoelectric tensor, the beam bends in the opposite direction (clockwise). This finding aligns with the results reported in [23].

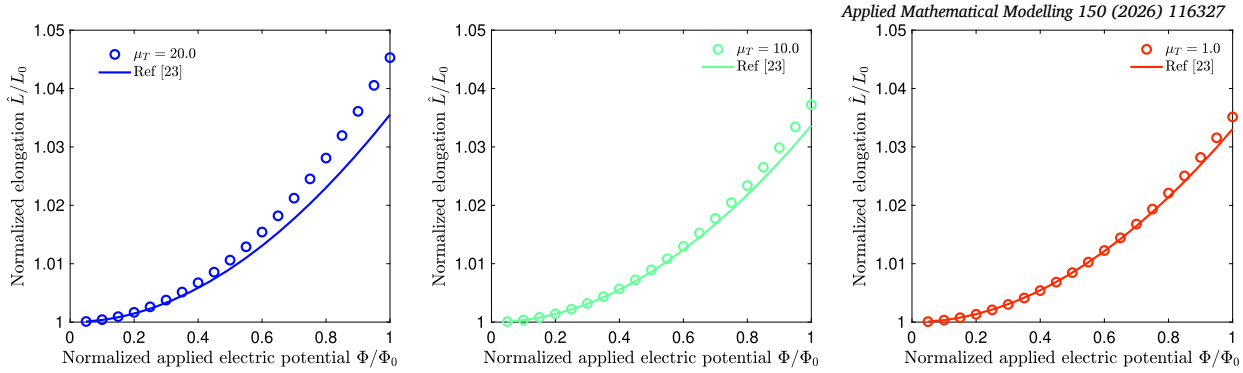

Fig. 7. Normalized elongation of the beam under an increasing applied electric potential. $\Phi_0 = 1$ [kV]. Unit of μ_T: [nC/m].

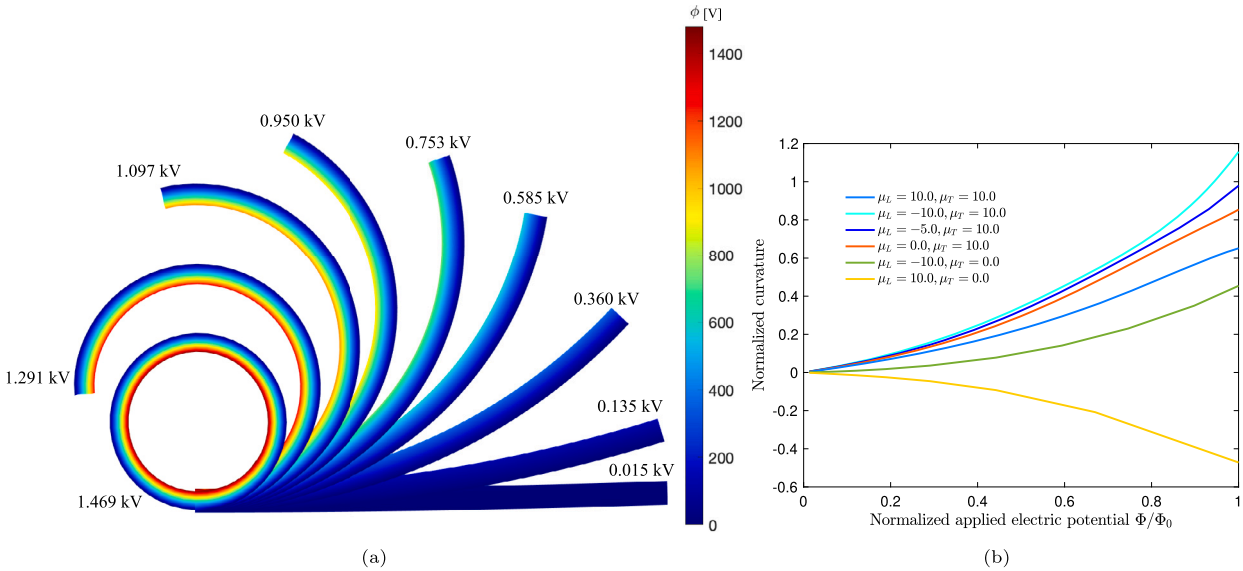

Fig. 8. Screenshots on deformed configuration and electric distribution under incrementally applied electric loading on the top edge with $\mu_L = 0$ and $\mu_T = 10\,\text{nC/m}$. (b) Evolution of the normalized curvature with the normalized electric loading. $\Phi_0 = 1.5$ [kV].

6. Numerical examples on dielectric solid immersed in free space

6.1. Dielectric bulk in free space

This section investigates problems concerning dielectric solids immersed in free space. It includes a well-established problem, as presented by Vu and Steinmann [42], which serves to verify the proposed framework. A square plate with a square hole at center is considered to be immersed in the free space, as shown in Fig. 9. To facilitate simulation, the infinite outer free space is truncated. The dimension of the truncated outer free space, the plate and the inner free space are $120\,\mu\text{m} \times 120\,\mu\text{m}$, $60\,\mu\text{m} \times 60\,\mu\text{m}$, and $30\,\mu\text{m} \times 30\,\mu\text{m}$, respectively. Two electrodes, with applied electric potential $+\boldsymbol{\Phi}_a$ and $-\boldsymbol{\Phi}_a$, are attached to the upper and lower edge of the plate, forming a closed circuit, where $\boldsymbol{\Phi}_a = 500\,\text{V}$. In this setup, the lower-left corner of the plate is fixed. Vertical displacements are restrained on the upper and lower edges of the plate within specific ranges: for $-30\,\mu\text{m} \le x \le -24\,\mu\text{m}$ and $+24\,\mu\text{m} \le x \le +30\,\mu\text{m}$, taking the center point as the origin. Fig. 9 also illustrates the IGA mesh used in the simulation. Both the outer free space and the plate are composed of multi-patch IGA meshes.

To align with numerical examples in [42], for this particular case the electric Gibbs free energy density of the material is tailored into

$$\bar{\Psi}^{\text{Gib}}_{\text{bulk}}(\boldsymbol{\mathcal{E}}, \boldsymbol{E}) = \Psi^{\text{Elast}}(\boldsymbol{\mathcal{E}}) + \alpha \boldsymbol{I} : \boldsymbol{E} \otimes \boldsymbol{E} + \beta \mathbf{C} : \boldsymbol{E} \otimes \boldsymbol{E} - \frac{1}{2}\epsilon J \mathbf{C}^{-1} : \boldsymbol{E} \otimes \boldsymbol{E}, \tag{56}$$

where Neo-Hookean material model is used for the determination of Ψ^{Elast} with Lamé constants $\hat{\lambda} = 0.06\,\text{MPa}$ and $\hat{\mu} = 0.05\,\text{MPa}$, $\alpha = 0.2\epsilon_0$ and $\beta = 2\epsilon_0$ are material constants and $\epsilon = 5\epsilon_0$. Note that the electromechanical coupling effects (piezoelectricity and flexoelectricity) are not considered in this case. The two extra energy terms are constructed based on the invariants $I_4 := \boldsymbol{I} : \boldsymbol{E} \otimes \boldsymbol{E}$ and $I_5 := \mathbf{C} : \boldsymbol{E} \otimes \boldsymbol{E}$ [42].

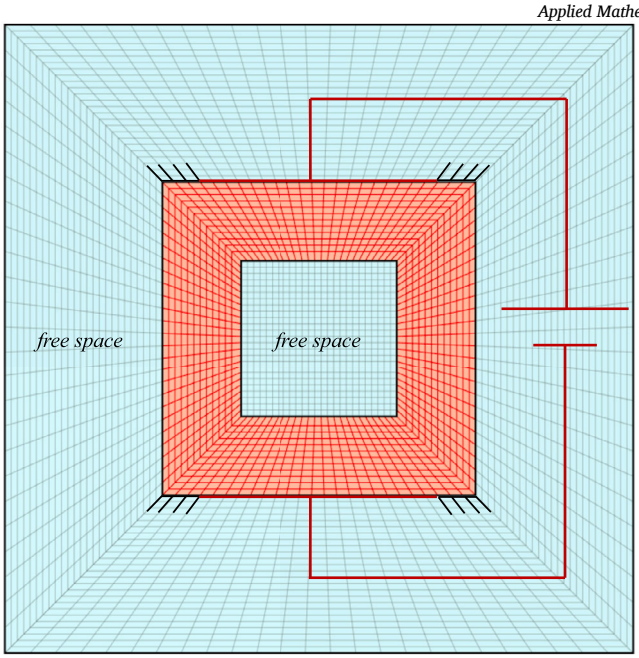

Fig. 9. IGA mesh exhibiting the bulk (red) and the free space (blue).

When modeling free space, a key consideration is the absence of elastic bonds among the nodes representing air (or vacuum). This characteristic renders the displacement of these degrees of freedom extremely sensitive to even slight external stimuli, often leading to numerical instabilities. To address this challenge effectively, the energy density functional for free space is modified as suggested by Ortigosa et al. [64]. This modification ensures stable simulation results by accounting for the unique nature of free space in the computational model.

$$\bar{\Psi}_{\text{space}}(\boldsymbol{\mathcal{E}}, \boldsymbol{E}) = \frac{\gamma}{2}(\mathbf{F}-\mathbf{I}) : \boldsymbol{C}_0 : (\mathbf{F}-\mathbf{I}) - \frac{1}{2}\epsilon_0(\boldsymbol{E}\cdot\boldsymbol{E}). \tag{57}$$

The first term in (57) represents a pseudoelastic energy term, designed to ensure smooth interpolation of energy between the bulk material and the free space. This is achieved by using a dimensionless coefficient $\gamma = 10^{-15}$ and $\boldsymbol{C}_0$, the fourth-order linear elasticity tensor, which can be numerically determined by evaluating the elasticity tensor of the bulk material in its undeformed state, where $\mathbf{F} = \mathbf{I}$. Regarding the second term in (28), a notable modification compared to the original functional (28) is the removal of the dependency on the deformation gradient. This adaptation is necessary due to the high non-convexity of the original energy functional with respect to the deformation gradient, leading to instability as discussed in [64]. Therefore, we use this stable version of the energy functional for free space (57) in both this and the following sections. It is important to note that this simplification might lead to accuracy losses in evaluating the Maxwell stress in free space. However, as suggested in [44], the difference between the two formulations in post-evaluation tests falls within an acceptable tolerance.

The simulation results are plotted in Fig. 10. In addition to the results for the plate with its surrounding free space, results for a single plate under identical boundary conditions and electric charge are presented for comparison. It is apparent that the material exhibits increased deformation when the influence of free space is considered. For a more detailed analysis, the vertical displacements along the top edge of the bulk material in both scenarios are extracted and illustrated in Fig. 11(a). These results align closely with those reported in previous literature [42,44]. Furthermore, the findings underscore the increased importance of considering free space in the context of finite deformation. This is evident as the results derived from a small electric charge display a smaller difference between the two scenarios, as shown in Fig. 11(b). Indeed, the Maxwell stress is considered significant only for soft materials with Young's modulus at the order of 0.1 GPa, where the Maxwell stress before electric breakdown can account for around 1% strain [19].

6.2. Flexoelectric beam in free space

A novel case study investigates the bending of a flexoelectric beam in free space, subject to an external electric field applied at a distance. This setup is depicted in Fig. 12. The free space surrounding the beam is truncated to dimensions of $100\,\mu\text{m} \times 80\,\mu\text{m}$ while the beam itself measures $50\,\mu\text{m} \times 10\,\mu\text{m}$. Constant electric potentials, $+\boldsymbol{\Phi}_a$ and $-\boldsymbol{\Phi}_a$, are applied to the top and bottom edges of the truncated free space, respectively, creating a vertical electric field within it. Initially, the beam is positioned horizontally, with its center point aligned with that of the truncated free space. The material parameters for the beam in the simulation include Young's modulus $Y = 1\,\text{MPa}$, Poisson's ratio $\nu = 0.1$, dielectric constant $\epsilon = 5\epsilon_0$, transversal flexoelectric coefficient $\mu_T = 10\,\text{nC/m}$, and material length parameter $l_s = 0.1\,\mu\text{m}$ for the strain gradient elasticity. The piezoelectric effect is not considered in this scenario.

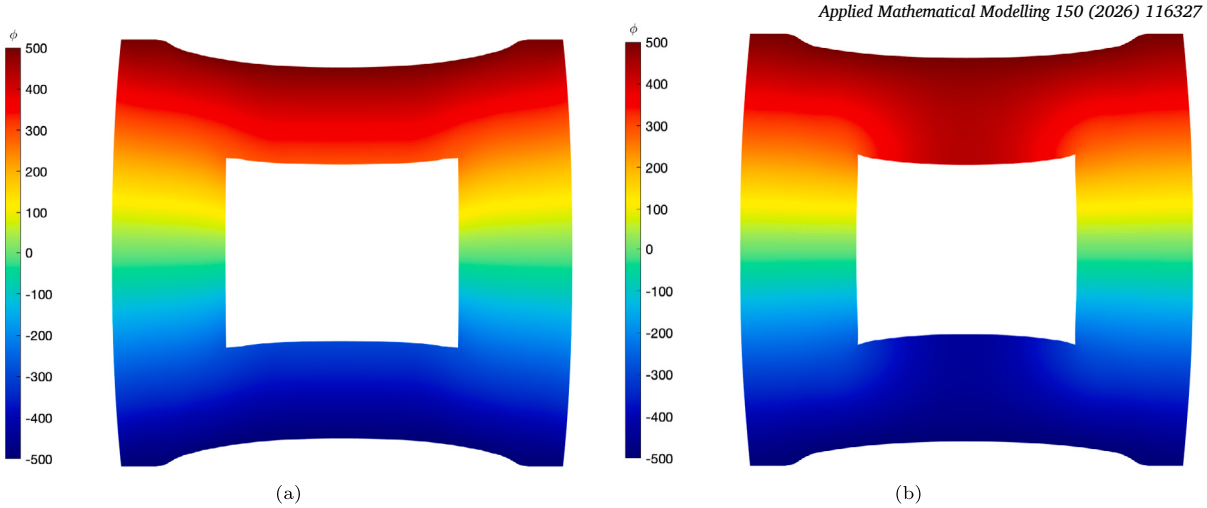

Fig. 10. Distribution of electric potential in deformed configuration for (a) bulk in free space; (b) bulk only. Unit: [V].

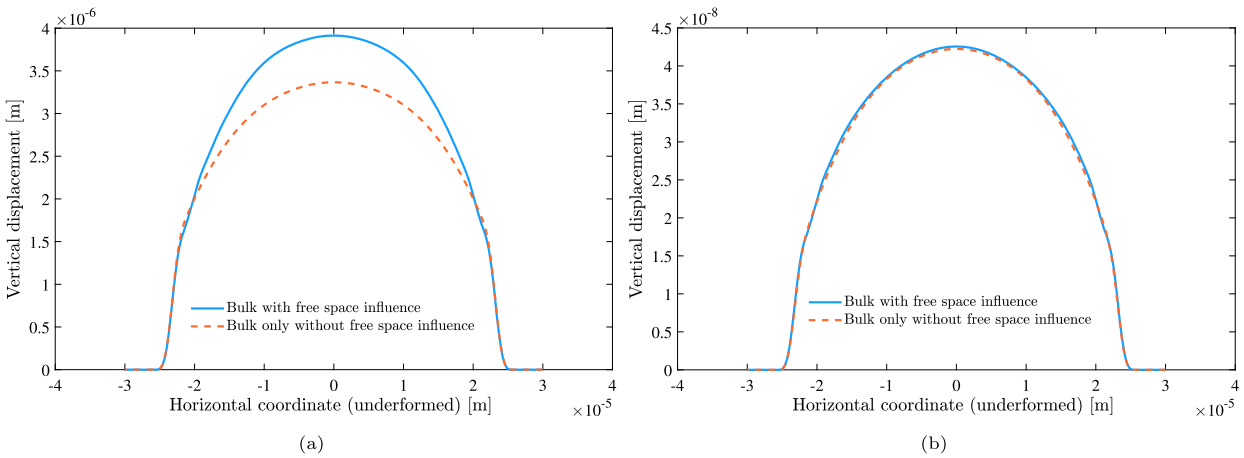

Fig. 11. Distribution of vertical displacement on the top edge of the bulk under electric charge (a) $\Phi_a = 500\,\mathrm{V}$; (b) $\Phi_a = 50\,\mathrm{V}$.

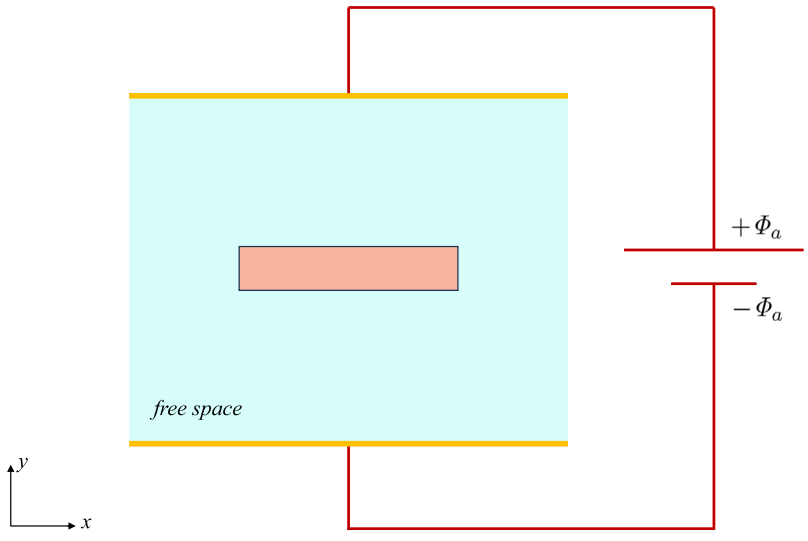

Fig. 12. Schematic of a beam immersed in the free space with electric potential applied at far field.

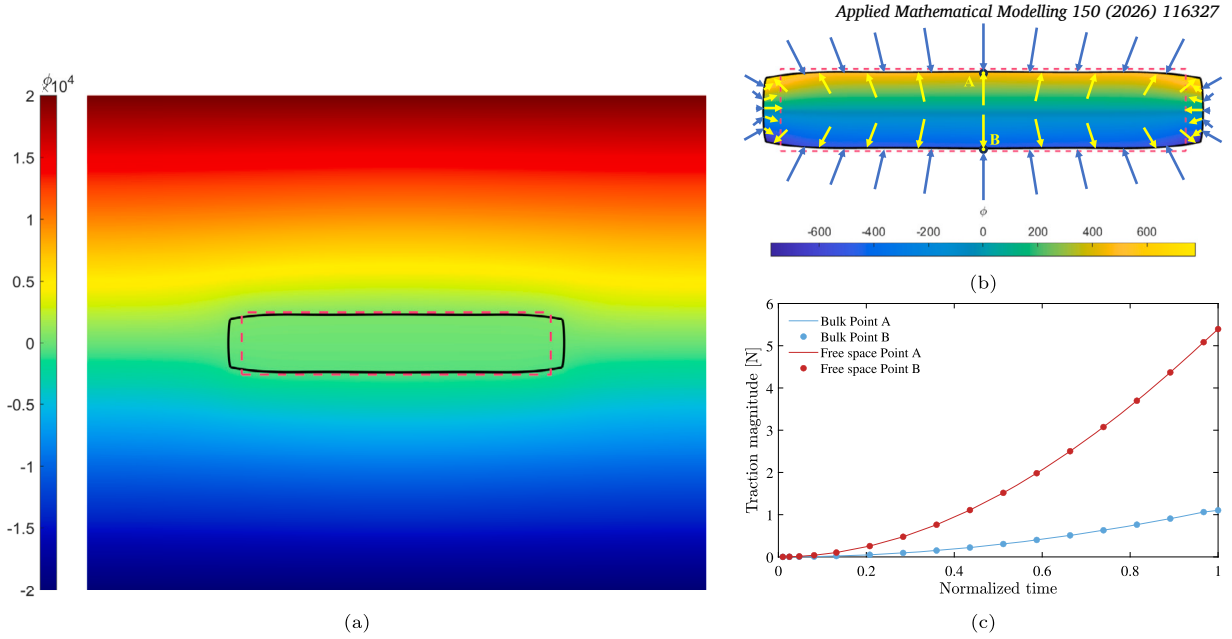

Fig. 13. (a) Electric potential distribution of the computing area; (b) schematic of traction forces due to the Maxwell stress; (c) magnitude of traction forces due to the Maxwell stress with respect to the normalized time. $\boldsymbol{\Phi}_a = 20\,\mathrm{kV}$ and $\epsilon = 5\epsilon_0$. The dashed boundary indicates the initial state.

The mechanical boundary conditions are as follows: the top and bottom edges of the truncated free space are fixed, while the remaining edges are free. The vertical midline across the beam's thickness is constrained in the x direction, and only the center point is additionally restrained in the y direction to prevent rigid body motion. All edges of the beam are traction-free.

The impact of the Maxwell stress effect is firstly examined by setting the flexoelectric coefficient to zero and the applied electric potential $\boldsymbol{\Phi}_a$ to 20 kV. Consequently, the beam elongates in the length direction and shortens in the thickness direction, as shown in Fig. 13(a), where the dashed red boundary represents the beam's initial configuration. This phenomenon aligns with experimental evidence reported in the literature [28,30,65]. Furthermore, the presence of the dielectric modifies the distribution of electric potential throughout the computing area, reducing the potential gradient around itself. In the absence of a dielectric in the free space or if its dielectric constant is equal to ϵ_0, the electric potential would typically decrease linearly from the top to the bottom edge. However, to satisfy the jump condition (9) at the interface between the dielectric and free space, the electric field inside the dielectric becomes smaller than that outside. This observation suggests that the Maxwell stress near the interface in the free space is greater than that within the dielectric, as per (36) and (42). To corroborate this hypothesis, traction forces attributable to Maxwell stress are evaluated on both sides of the free space-dielectric interface. These forces are depicted in Fig. 13(b), where their magnitudes are scaled for visualization, but their directions and reaction locations are accurately represented. It is observed that the traction force due to Maxwell stress in free space indeed exceeds that within the dielectric, leading to a net compressive force along the beam. In Fig. 13(b), two points on the interface, labeled as point 'A' and point 'B', are examined further. Due to the symmetric conditions of the setup, the Maxwell-induced traction forces at these points possess only vertical components. The evolution of these forces, relative to normalized time, is depicted in Fig. 13(c). Given the symmetric deformation of the beam with respect to its horizontal midline, the magnitudes of the Maxwell-induced traction forces at points 'A' and 'B' are identical when measured on the same side of the interface. It is observed that the net compression forces, which result from the difference in Maxwell stress across the interface, escalate more rapidly than a linear relationship with respect to normalized time.

Incorporating the flexoelectric effect, the beam exhibits bending in response to the electric field, as depicted in Fig. 14. Besides, the convergence analysis is provided in Fig. 15. The figures on the left side of Fig. 14 illustrate the electric field in the vertical direction, as the horizontal component is insignificant in comparison. The results demonstrate a decrease in the electric field intensity within the beam with an increase in the dielectric constant, leading to a reduced bending extent. This phenomenon is attributed to the fact that the double stress driving the bending motion is directly influenced by the electric field, as established in (31). Upon bending, the magnitude of traction forces due to Maxwell stress at points 'A' and 'B' on both the free space and dielectric sides begins to diverge, as shown on the right side of Fig. 14. This divergence indicates a loss of symmetry relative to the horizontal midline. However, this symmetry can be partially restored by employing a high dielectric constant for the material. In such scenarios, as illustrated in Fig. 14(e)(f), the mechanical response of the beam becomes less distinct, suggesting that the beam gets 'stiffened' with an increased dielectric constant. Consequently, it becomes less responsive to external electrical or mechanical stimuli, and the influence of the free space on its behavior becomes minimal.

The influence of the Maxwell stress effect is further investigated by comparing the results obtained using the proposed numerical framework with those from linear flexoelectricity. In the theory of linear flexoelectricity, the state variables are not deformation-dependent. The variations in dielectric and flexoelectric energy with respect to deformation become zero, and thus the Maxwell stress

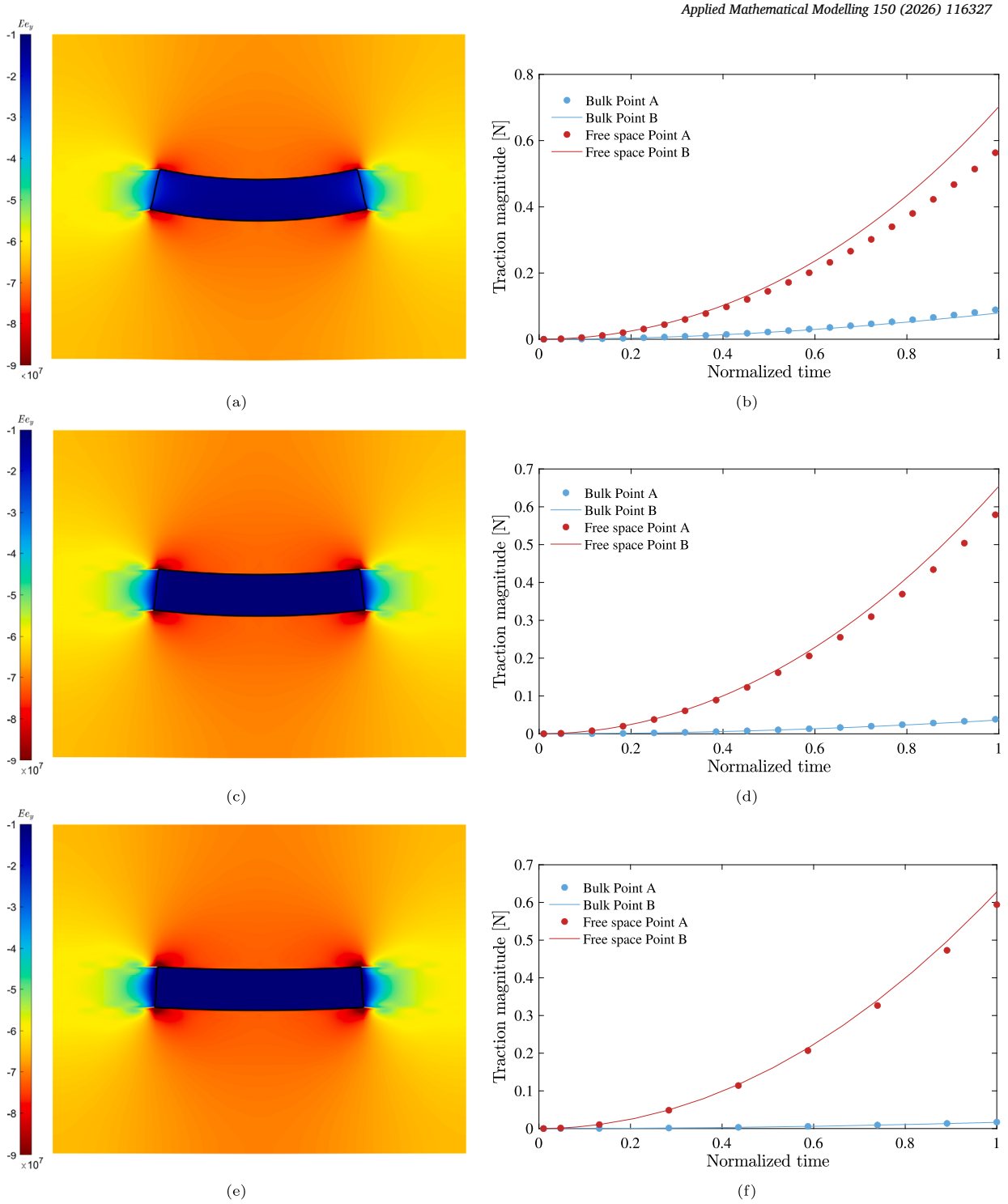

Fig. 14. Schematic of electric field distribution and beam bending (a)(c)(e) and magnitude of traction forces due to the Maxwell stress with respect to the normalized time (b)(d)(f). The applied electric potential $\Phi_a = 5\,\mathrm{kV}$ and dielectric constant for (a)(b) $\epsilon = 5\epsilon_0$; (c)(d) $\epsilon = 10\epsilon_0$; (e)(f) $\epsilon = 20\epsilon_0$. Unit of E_{e_y}: [V/m].

vanishes. Using the same material parameters as in linear elasticity, the differences in displacement and electric potential distribution of the dielectric solid are quantified, as shown in Fig. 16. A total of 50×50 points are equidistantly sampled in the parametric space, and the difference is computed in percentage with increasing applied voltage up to 15 [kV]. It is observed that the differences in both displacement and electric potential increase steadily with the applied voltage. When the applied voltage reaches 10 kV, the Maxwell

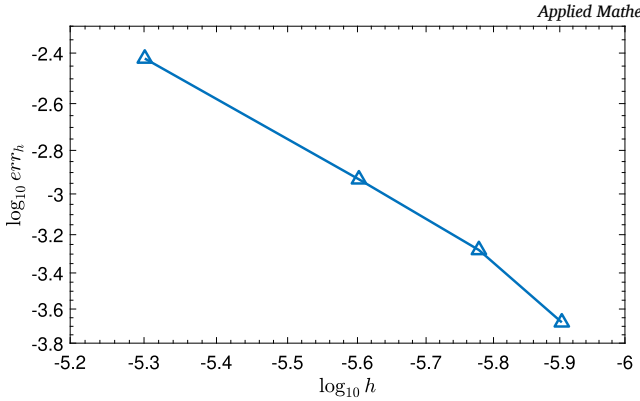

Fig. 15. Convergence analysis of $err_h = |\Phi - \Phi_{ref}|/|\Phi_{ref}|$ with respect to the element size h. Φ_{ref} is taken from the results of $h = 10^{-6}$ [m].

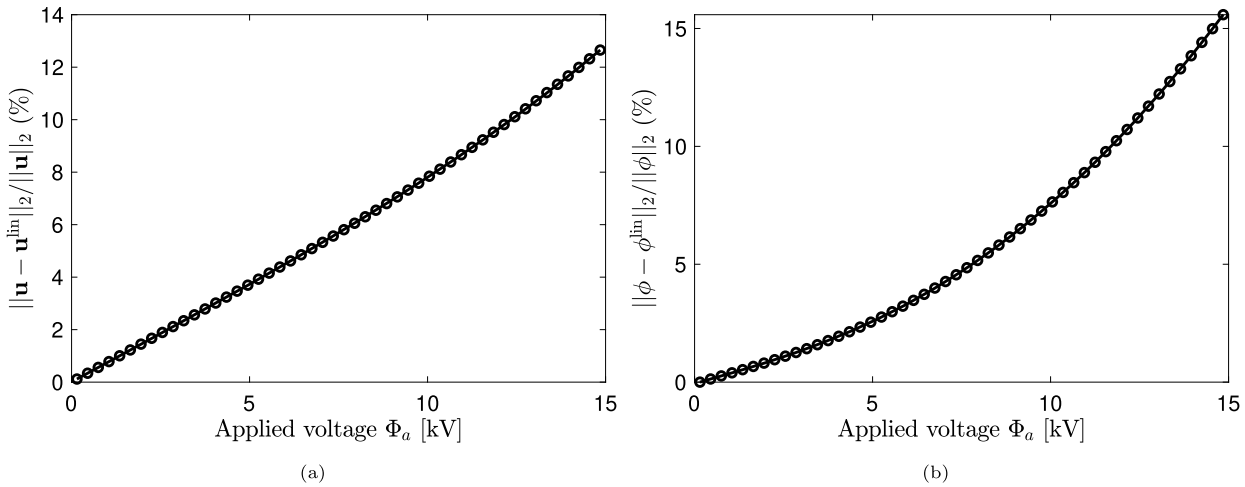

Fig. 16. The influence of Maxwell stress effect in the results difference in percentage of (a) displacement and (b) electric potential by comparing results obtained using the proposed numerical framework and those using linear flexoelectricity.

stress effect becomes significant, accounting for around 8% of the deformation and electric potential. The influence of the Maxwell stress effect on deformation is illustrated in Fig. 17, where the dielectric is further compressed in the direction of the electric field as a result of the Maxwell stress compared with linear flexoelectricity results.

Finally, we would like to note that the use of the pure Lagrangian frame in this study may limit the extent of large deformations in simulations involving free space, due to the potential for significant mesh distortion. Despite these computational challenges, it's worth noting that these limitations do not detract from the validity of our findings, as the trends observed when varying control parameters remain consistent and reasonable. Nevertheless, techniques that can potentially overcome these drawbacks, e.g. adopting an Eulerian frame, will be the focus of our future investigations.

6.3. Bursting drops in high voltage electric field

In this final example, we aim to elucidate the numerical simulation of a well-documented physical phenomenon—the bursting drops under a high voltage electric field, leading to the formation of a Taylor cone, as observed in *in situ* experiments [66]. Numerical modeling approaches to this phenomenon diverge, generally falling into two distinct categories based on their problem settings. The first category models the drop as a dielectric solid within free space [21,22], as illustrated in Fig. 18(a). In contrast, the second category depicts a conductive liquid drop immersed in a dielectric polymer [67,68], as shown in Fig. 18(b). It is critical to note that the approaches accurately capturing the bursting drop phenomenon align with the second category. Firstly, considering the conductive nature of water drops, the electric field inside such a drop is effectively neutralized, leading to zero magnitude. Modeling the drop as a dielectric solid inadvertently introduces an internal non-zero electric field, contradicting experimental evidence. Additionally, insights from the previous section suggest that Maxwell stress effect tends to compress the dielectric solid in the direction of the electric field rather than stretching it along this field.

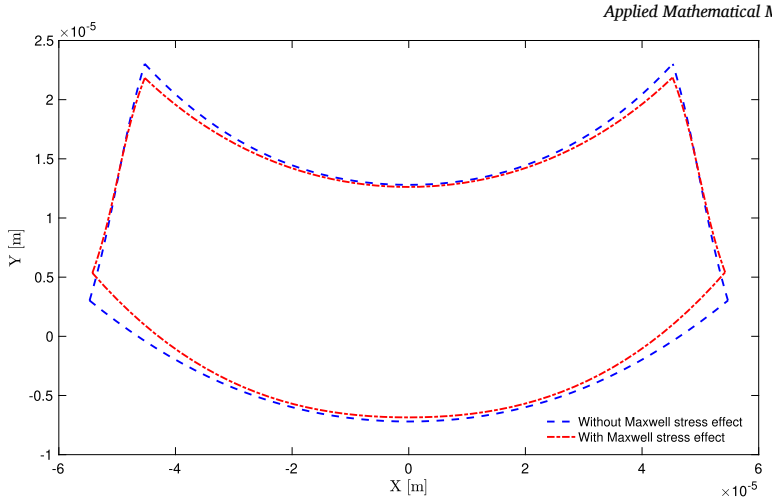

Fig. 17. Deformation of the dielectric solid at $\Phi_a = 10$ [kV].

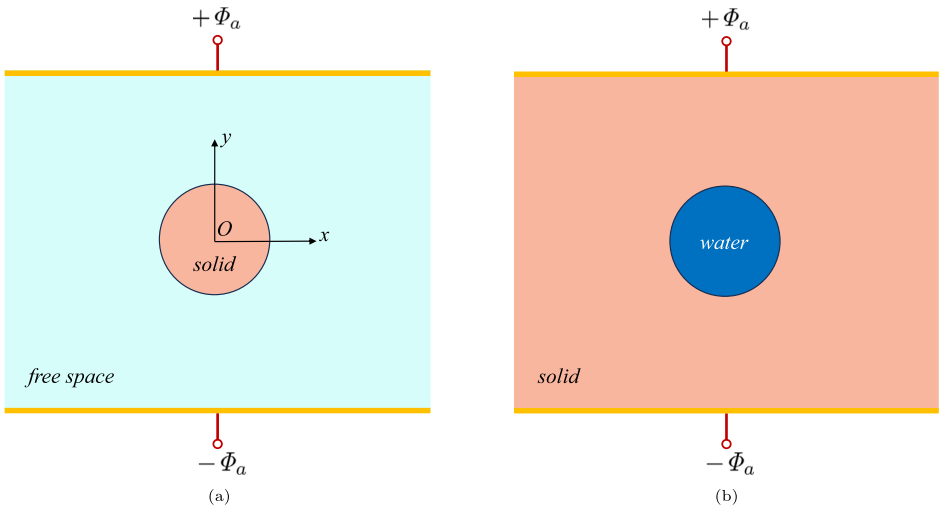

Fig. 18. Problem configurations of the bursting drop simulation. (a) A dielectric solid with a droplet shape immersed in the surrounding free space. (b) A water drop with surrounding dielectric solid medium. Dimension of the surrounding medium: 1.3 [mm]×1.3 [mm], radius of the drop: 0.3 [mm]. Material parameters for the solid: Neo-hookean material with $Y = 0.01$ [MPa] and $\nu = 0.4$ and $\epsilon = 5\epsilon_0$.

Simulation results using the first approach are presented in Fig. 19(b), where the droplet solid is observed to compress vertically rather than stretch under the electric field, which is in accordance with the experimental results of the deformation of a silicon oil in vertical electric field, as shown in Fig. 19(a). On the contrary, adopting the configuration outlined in Fig. 18(b) yields results in alignment with experimental findings shown in Fig. 20. Under such condition, the water drop elongates along the applied electric field, forming sharp tips at critically high external voltages.

7. Conclusions

In this work, we have developed a complete variational framework for modeling nonlinear flexoelectricity in dielectric soft materials, critically accounting for the interaction with the surrounding free space. By deriving the strong equilibrium equations from a total energy functional, our approach ensures that the Maxwell stress emerges naturally without ad-hoc assumptions, and is thus variationally consistent. The robust Isogeometric analysis framework was validated against established benchmarks in both infinitesimal and finite deformation scenarios before being used to investigate novel phenomena involving surrounding free space.

The primary contributions and key takeaways of this study are:

- Our approach derives the Maxwell stress tensor directly from the variational principle, providing a consistent formulation for flexoelectric materials undergoing finite deformation. This Maxwell stress naturally includes contributions from flexoelectricity.

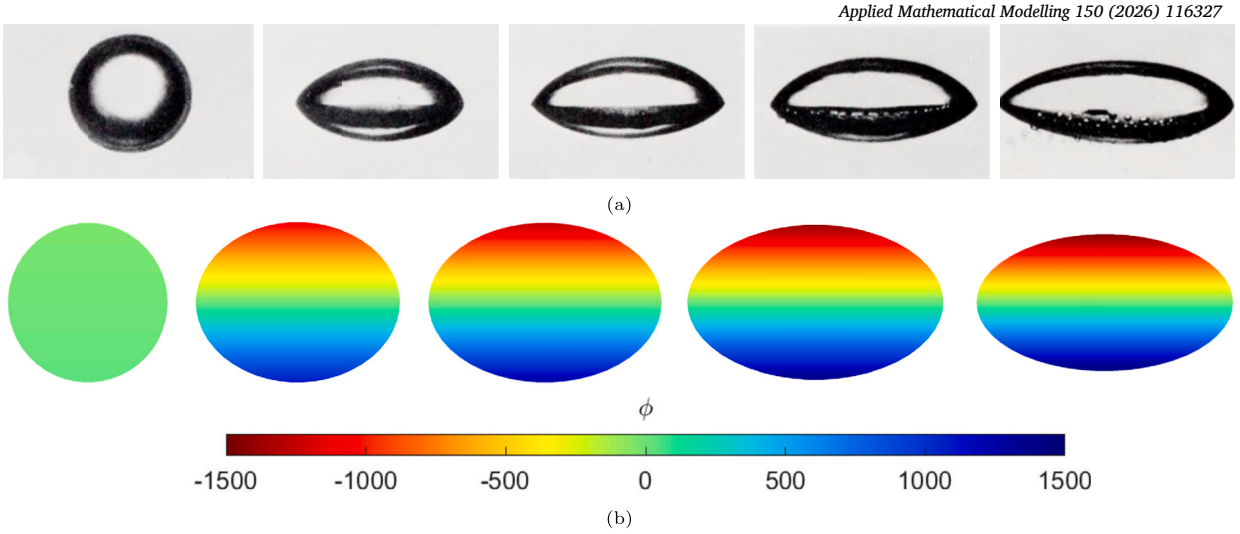

Fig. 19. (a) The photographs of a drop of silicon oil in castor oil in constant vertical electric fields [69], figure adopted with permission from the Royal Society; (b) Deformation of the droplet-shape solid upon increasing external electric field. Boundary conditions: upper and lower edge of the free space is fixed, vertical mid-line of the solid is fixed in the x-direction and only the center point is also fixed in the y-direction. Mesh is refined by 5-level h-refinement. $\boldsymbol{\Phi}_a = 40$ [kV].

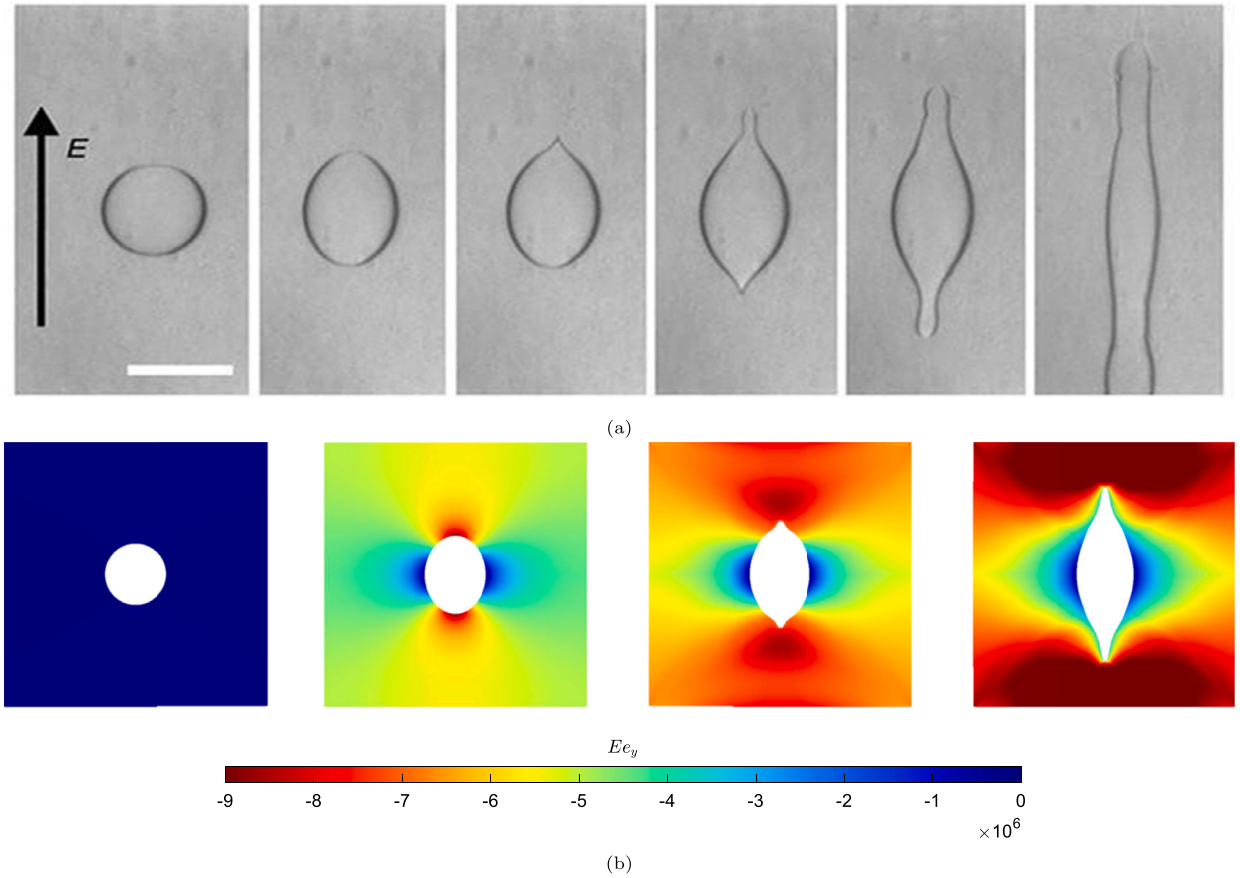

Fig. 20. (a) Morphological instability of a drop of conductive liquid in a dielectric polymer under electric fields [66], licensed under CC BY 4.0 https://creativecommons.org/version4/; (b) Deformation of the water drop upon increasing external electric field. Boundary conditions: all four outer edges are fixed and the electric potential of the inner circle is prescribed zero. Mesh is refined by 5-level h-refinement. $\boldsymbol{\Phi}_a = 10$ [kV].

- The interaction with the surrounding free space was shown to significantly amplify the deformation of soft dielectrics. We demonstrated that a net compressive traction is generated on the dielectric's surface in the direction of the electric field, arising from the larger Maxwell stress in the free space compared to that within the material.
- A higher dielectric constant makes the material mechanically "stiffened" in response to external electric loads. This effect diminishes the material's deformation and mitigates the influence of the surrounding free space, which provides insights for the design of electro-active devices.
- The framework successfully simulates the distinct behaviors of dielectric solids (which are compressed) and conductive liquid drops (which form Taylor cones) in an electric field, clarifying the physical mechanisms often grouped under the "bursting drop" phenomenon.

In addition, we identify the following open problems and challenges that could lead to significant new findings:

- The pure Lagrangian framework used in this study faces challenges with severe mesh distortion when modeling very large deformations, particularly in the free space domain. A future direction is the development of an Arbitrary Lagrangian-Eulerian (ALE) or a pure Eulerian framework to overcome these limitations.
- The theoretically rigorous electric energy functional for free space depends on the deformation gradient, leading to a highly non-convex formulation that causes severe numerical instabilities when simulating the mechanically compliant free space domain. While this work uses a stable energy functional, it may introduce inaccuracies at the interface. A significant challenge remains in developing fully-coupled formulations or stabilized numerical methods that are both theoretically accurate and numerically robust for large deformations of free space.

CRediT authorship contribution statement

Xiaoying Zhuang: Writing – review & editing, Supervision, Funding acquisition, Conceptualization. **Han Hu:** Writing – review & editing, Writing – original draft, Software, Methodology, Investigation, Formal analysis, Conceptualization. **S.S. Nanthakumar:** Writing – review & editing, Investigation, Formal analysis. **Quoc-Thai Tran:** Writing – review & editing, Methodology, Investigation. **Yanpeng Gong:** Writing – review & editing, Methodology, Investigation. **Timon Rabczuk:** Writing – review & editing, Supervision.

Declaration of competing interest

The authors declare that they have no known competing financial interests or personal relationships that could have appeared to influence the work reported in this paper.

Acknowledgements

Dr. Hu acknowledges Dr. David Codony for helpful email discussions.

Appendix A. Detailed derivation of the last integral of (34)

$$
\begin{aligned}
&\int_{\partial\mathcal{B}_0} \frac{1}{2}\left[\Sigma_{IJK}\,\chi_{k,I}\,\delta\chi_{k,J} + \Sigma_{IJK}\,\chi_{k,J}\,\delta\chi_{k,I}\right] N_K \,\mathrm{d}\Gamma \\
&= \int_{\partial\mathcal{B}_0} \frac{1}{2}\Sigma_{IJK} N_K \left[\chi_{k,I}(D_J^{(t)}\,\delta\chi_k + N_J D^{(n)}\,\delta\chi_k) + \chi_{k,J}(D_I^{(t)}\,\delta\chi_k + N_I D^{(n)}\,\delta\chi_k)\right] \mathrm{d}\Gamma \\
&= \int_{\partial\mathcal{B}_0} \frac{1}{2}\left[D_J^{(t)}\left(\Sigma_{IJK} N_K\,\chi_{k,I}\,\delta\chi_k\right) - N_K D_J^{(t)}\Sigma_{IJK}\,\chi_{k,I}\,\delta\chi_k - D_J^{(t)} N_K \Sigma_{IJK}\,\chi_{k,I}\,\delta\chi_k\right] \mathrm{d}\Gamma \\
&\quad + \int_{\partial\mathcal{B}_0} \frac{1}{2}\left[D_I^{(t)}\left(\Sigma_{IJK} N_K\,\chi_{k,J}\,\delta\chi_k\right) - N_K D_I^{(t)}\Sigma_{IJK}\,\chi_{k,J}\,\delta\chi_k - D_I^{(t)} N_K \Sigma_{IJK}\,\chi_{k,J}\,\delta\chi_k\right] \mathrm{d}\Gamma \\
&\quad + \int_{\partial\mathcal{B}_0} \frac{1}{2}\Sigma_{IJK} N_K \left(\chi_{k,I} N_J D^{(n)}\,\delta\chi_k + \chi_{k,J} N_I D^{(n)}\,\delta\chi_k\right) \mathrm{d}\Gamma \qquad \text{(A.1)} \\
&= \int_{\partial\mathcal{B}_0} \frac{1}{2}\Big[D_L^{(t)} N_L N_J N_K \Sigma_{IJK}\,\chi_{k,I}\,\delta\chi_k + N_Q \theta_{QPM}\partial_P(\theta_{MLJ} N_L N_K \Sigma_{IJK}\,\chi_{k,I}\,\delta\chi_k) \\
&\quad + D_L^{(t)} N_L N_I N_K \Sigma_{IJK}\,\chi_{k,J}\,\delta\chi_k + N_Q \theta_{QPM}\partial_P(\theta_{MLI} N_L N_K \Sigma_{IJK}\,\chi_{k,J}\,\delta\chi_k) \\
&\quad - (D_J^{(t)}\Sigma_{IJK}\,\chi_{k,I} + D_I^{(t)}\Sigma_{IJK}\,\chi_{k,J}) N_K\,\delta\chi_k - (D_J^{(t)} N_K\,\chi_{k,I} + D_I^{(t)} N_K\,\chi_{k,J})\Sigma_{IJK}\,\delta\chi_k
\end{aligned}
$$

$$+\int_{\partial\mathcal{B}_0}\frac{1}{2}\Sigma_{IJK}N_K\left(\chi_{k,I}N_J+\chi_{k,J}N_I\right)D^{(n)}\,\delta\chi_k\Big]\,\mathrm{d}\Gamma$$
$$=\int_{\partial\mathcal{B}_0}\widetilde{T}_k^{(t)}\,\delta\chi_k\,\mathrm{d}\Gamma+\int_{\partial\mathcal{B}_0}\widetilde{T}_k^{(n)}D^{(n)}\,\delta\chi_k\,\mathrm{d}\Gamma,$$

where θ_{QPM} is the alternating tensor, and

$$\begin{aligned}\widetilde{T}_k^{(t)}&=\frac{1}{2}\big[\Sigma_{IJK}N_K(N_J\,\chi_{k,I}+N_I\,\chi_{k,J})D_L^{(t)}N_L-N_K(\chi_{k,I}D_J^{(t)}\Sigma_{IJK}+\chi_{k,J}D_I^{(t)}\Sigma_{IJK})\\&\quad-\Sigma_{IJK}(\chi_{k,I}D_J^{(t)}N_K+\chi_{k,J}D_I^{(t)}N_K)\big],\\\widetilde{T}_k^{(n)}&=\frac{1}{2}\Sigma_{IJK}N_K\left(\chi_{k,I}N_J+\chi_{k,J}N_I\right).\end{aligned}\tag{A.2}$$

Appendix B. Detailed derivation of the incremental change of $\mathcal{R}_{es}$

$$\begin{aligned}&\Delta\mathcal{R}_{es}(\chi,\Phi,\delta\chi,\delta\Phi;\Delta\chi,\Delta\Phi)=\frac{\partial R_{es}(\chi,\Phi,\delta\chi,\delta\Phi)}{\partial\chi}\Delta\chi+\frac{\partial R_{es}(\chi,\Phi,\delta\chi,\delta\Phi)}{\partial\phi}\Delta\phi\\&=\int_{\mathcal{B}_0}\Big\{(\widehat{S}_{IJ}+\widehat{S}_{IJ}^{\mathrm{MW}})(\Delta\delta)\mathcal{E}_{IJ}+\widehat{\Sigma}_{IJK}(\Delta\delta)\mathcal{G}_{IJK}+(\mathbb{A}_{IJKL}^{\mathrm{Mech}}+\mathbb{A}_{IJKL}^{\mathrm{Diele}}+\mathbb{A}_{IJKL}^{\mathrm{Flexo}}+\mathbb{A}_{IJKL}^{\mathrm{Piezo}})\,\delta\mathcal{E}_{IJ}\,\Delta\mathcal{E}_{KL}\\&\quad+\mathbb{B}_{IJKLMN}^{\mathrm{Mech}}\,\delta\mathcal{G}_{IJK}\,\Delta\mathcal{G}_{LMN}+(\mathbb{C}_{IJKLM}^{\mathrm{Mech}}+\mathbb{C}_{IJKLM}^{\mathrm{Flexo}})(\delta\mathcal{E}_{IJ}\,\Delta\mathcal{G}_{LMN}+\delta\mathcal{G}_{LMN}\,\Delta\mathcal{E}_{IJ})\\&\quad+\mathbb{D}_{IJ}^{\mathrm{Diele}}\,\delta E_I\,\Delta E_J+(\mathbb{E}_{IJK}^{\mathrm{Diele}}+\mathbb{E}_{IJK}^{\mathrm{Flexo}}+\mathbb{E}_{IJK}^{\mathrm{Piezo}})(\delta\mathcal{E}_{IJ}\,\Delta E_K+\delta E_K\,\Delta\mathcal{E}_{IJ})\\&\quad+\mathbb{F}_{IJKL}^{\mathrm{Flexo}}(\delta\mathcal{G}_{IJKL}\,\Delta E_L+\delta E_L\,\Delta\mathcal{G}_{IJKL})\Big\}\mathrm{d}V\end{aligned}\tag{B.1}$$

$$+\int_{\mathcal{B}_0'}\left\{S_{IJ}^{\mathrm{MWE}}(\Delta\delta)\mathcal{E}_{IJ}+\mathbb{G}_{IJKL}^{\mathrm{Elec}}\,\delta\mathcal{E}_{IJ}\,\Delta\mathcal{E}_{KL}+\mathbb{H}_{IJK}^{\mathrm{Elec}}\,(\delta\mathcal{E}_{IJ}\,\Delta E_K+\delta E_K\,\Delta\mathcal{E}_{IJ})+\mathbb{I}_{IJ}^{\mathrm{Elec}}\,\delta E_I\,\Delta E_J\right\}\mathrm{d}V,\tag{B.2}$$

where $\widehat{S}_{IJ}$, $\widehat{S}_{IJ}^{\mathrm{MW}}$ and $\widehat{\Sigma}_{IJK}$ represent the second Piola-Kirchhoff stress, the second Piola-Maxwell stress and the second Piola-Kirchhoff double stress after considering piezoelectric effect, respectively, and they are defined as

$$\begin{aligned}\widehat{S}_{IJ}&:=\frac{\partial\Psi^{\mathrm{Elast}}}{\partial\mathcal{E}_{IJ}}+\frac{J\mathfrak{C}_{MFIJ}}{2(\epsilon-\epsilon_0)}\big[\mu_{MABK}\mathcal{G}_{ABK}\,\mu_{FXYZ}\mathcal{G}_{XYZ}+2\mu_{MABK}\mathcal{G}_{ABK}\,\eta_{FXY}\,\mathcal{E}_{XY}\\&\quad+\eta_{MAB}\,\mathcal{E}_{AB}\,\eta_{FXY}\,\mathcal{E}_{XY}\big]-JE_M\,C_{ML}^{-1}\eta_{LIJ}-\frac{J}{\epsilon-\epsilon_0}\mu_{MABK}\mathcal{G}_{ABK}\,C_{MF}^{-1}\eta_{FIJ}\\&\quad-\frac{J}{\epsilon-\epsilon_0}\eta_{MAB}\,\mathcal{E}_{AB}\,C_{MF}^{-1}\eta_{FIJ},\end{aligned}\tag{B.3}$$

$$\widehat{S}_{IJ}^{\mathrm{MW}}:=J\mathfrak{C}_{MFIJ}\big(\frac{1}{2}\epsilon E_M\,E_F+E_M\,\mu_{FABK}\mathcal{G}_{ABK}+E_M\,\eta_{FAB}\,\mathcal{E}_{AB}\big),\tag{B.4}$$

$$\begin{aligned}\widehat{\Sigma}_{IJK}&:=h_{IJKLMN}\mathcal{G}_{LMN}-JE_M\,C_{MF}^{-1}\mu_{FIJK}-\frac{J}{(\epsilon-\epsilon_0)}\mu_{MABC}\mathcal{G}_{ABC}\,C_{MF}^{-1}\mu_{FIJK}\\&\quad-\frac{J}{(\epsilon-\epsilon_0)}\mu_{MIJK}\,C_{MF}^{-1}\eta_{FAB}\,\mathcal{E}_{AB},\end{aligned}\tag{B.5}$$

where $\Delta\chi$ and $\Delta\Phi$ indicate the incremental change of χ and Φ, respectively, and

$$\begin{aligned}&\Delta F_{iI}(\chi;\Delta\chi):=\Delta\chi_{i,I},\qquad\Delta\mathcal{F}_{iIJ}(\chi;\Delta\chi):=\Delta\chi_{i,IJ},\qquad\Delta\mathcal{E}_{IJ}(\chi;\Delta\chi):=\operatorname*{symm}_{IJ}(\chi_{k,J}\,\Delta\chi_{k,I}),\\&\Delta\mathcal{G}_{IJK}(\chi;\Delta\chi):=\operatorname*{symm}_{IJ}(\chi_{k,J}\,\Delta\chi_{k,IK}+\chi_{k,IK}\,\Delta\chi_{k,J}),\quad(\Delta\delta)\mathcal{E}_{IJ}(\chi;\Delta\chi):=\operatorname*{symm}_{IJ}(\Delta\chi_{k,I}\delta\chi_{k,J}),\\&(\Delta\delta)\mathcal{G}_{IJK}(\chi;\Delta\chi):=\operatorname*{symm}_{IJ}(\delta\chi_{k,J}\,\Delta\chi_{k,IK}+\delta\chi_{k,IK}\,\Delta\chi_{k,J}),\quad\Delta E_L(\Phi;\Delta\Phi):=-\Delta\Phi_{,L}.\end{aligned}\tag{B.6}$$

The tangent stiffness matrix in (50) is composed by material tensors in the right hand side of (B.1), defined as

$$\begin{aligned}\mathbb{A}_{IJKL}^{\mathrm{Mech}}&:=\frac{\partial^2\bar{\Psi}^{\mathrm{Mech}}}{\partial\mathcal{E}_{IJ}\,\partial\mathcal{E}_{KL}}=\frac{\partial^2\Psi^{\mathrm{Elast}}}{\partial\mathcal{E}_{IJ}\,\partial\mathcal{E}_{KL}}+\frac{J}{\epsilon-\epsilon_0}\big(\frac{1}{2}\mathscr{C}_{MFIJKL}\mu_{MABC}\,\mathcal{G}_{ABC}\,\mu_{FXYZ}\,\mathcal{G}_{XYZ}\\&\quad+\frac{1}{2}\mathscr{C}_{MFIJKL}\eta_{MAB}\,\mathcal{E}_{AB}\,\eta_{FCD}\,\mathcal{E}_{CD}+\mathscr{C}_{MFIJKL}\mu_{MABK}\,\mathcal{G}_{ABK}\,\eta_{FCD}\,\mathcal{E}_{CD}\\&\quad+\mathfrak{C}_{MFKL}\,\mu_{MABC}\,\mathcal{G}_{ABC}\,\eta_{FIJ}+\mathfrak{C}_{MFIJ}\,\mu_{MABC}\,\mathcal{G}_{ABC}\,\eta_{FKL}\\&\quad+\mathfrak{C}_{MFKL}\,\eta_{MAB}\,\mathcal{E}_{AB}\,\eta_{FIJ}+\mathfrak{C}_{MFIJ}\,\eta_{MAB}\,\mathcal{E}_{AB}\,\eta_{FKL}-\eta_{MKL}C_{MF}^{-1}\eta_{FIJ}\big),\end{aligned}\tag{B.7}$$

$$\mathbb{A}^{\text{Diele}}_{IJKL} := \frac{\partial^2(\bar{\Psi}^{\text{Diele}} - \bar{\Psi}^{\text{Elec}})}{\partial \mathcal{E}_{IJ}\,\partial \mathcal{E}_{KL}} = \frac{1}{2} J \epsilon \mathscr{C}_{MFIJKL} E_M\, E_F, \tag{B.8}$$

$$\mathbb{A}^{\text{Flexo}}_{IJKL} := \frac{\partial^2 \bar{\Psi}^{\text{Flexo}}}{\partial \mathcal{E}_{IJ}\,\partial \mathcal{E}_{KL}} = J \mathscr{C}_{MFIJKL} E_M\, \mu_{FABC}\, \mathcal{G}_{ABC}, \tag{B.9}$$

$$\mathbb{A}^{\text{Piezo}}_{IJKL} := \frac{\partial^2 \bar{\Psi}^{\text{Piezo}}}{\partial \mathcal{E}_{IJ}\,\partial \mathcal{E}_{KL}} = J(\mathscr{C}_{MFIJKL} E_M\, \eta_{FAB}\, \mathcal{E}_{AB} + \mathfrak{C}_{MFKL}\, E_M\, \eta_{FIJ} + \mathfrak{C}_{MFIJ}\, E_M\, \eta_{FKL}), \tag{B.10}$$

$$\mathbb{B}^{\text{Mech}}_{IJKLMN} := \frac{\partial^2 \bar{\Psi}^{\text{Mech}}}{\partial \mathcal{G}_{IJK}\,\partial \mathcal{G}_{LMN}} = h_{IJKLMN} - \frac{J}{\epsilon - \epsilon_0} \mu_{ALMN}\, C^{-1}_{AB}\, \mu_{BIJK}, \tag{B.11}$$

$$\begin{aligned}\mathbb{C}^{\text{Mech}}_{IJKLM} := \frac{\partial^2 \bar{\Psi}^{\text{Mech}}}{\partial \mathcal{E}_{IJ}\,\partial \mathcal{G}_{KLM}} = \frac{J}{\epsilon - \epsilon_0}\big(&\mathfrak{C}_{ABIJ}\, \mu_{AKLM}\, \eta_{BXY}\, \mathcal{E}_{XY} - \mu_{AKLM}\, C^{-1}_{AB} \eta_{BIJ} \\ &+ \mathfrak{C}_{ABIJ}\, f_{AXYZ}\, \mathcal{G}_{XYZ}\, f_{BKLM}\big),\end{aligned} \tag{B.12}$$

$$\mathbb{C}^{\text{Flexo}}_{IJKLM} := \frac{\partial^2 \bar{\Psi}^{\text{Flexo}}}{\partial \mathcal{E}_{IJ}\,\partial \mathcal{G}_{KLM}} = J \mathfrak{C}_{ABIJ}\, E_A\, \mu_{BKLM}, \tag{B.13}$$

$$\mathbb{D}^{\text{Diele}}_{IJ} := \frac{\partial^2(\bar{\Psi}^{\text{Diele}} - \bar{\Psi}^{\text{Elec}})}{\partial E_I\,\partial E_J} = -J \epsilon\, C^{-1}_{IJ}, \tag{B.14}$$

$$\mathbb{E}^{\text{Diele}}_{IJK} := \frac{\partial^2 \bar{\Psi}^{\text{Diele}}}{\partial \mathcal{E}_{IJ}\,\partial E_K} = J \epsilon\, \mathfrak{C}_{KMIJ}\, E_M, \tag{B.15}$$

$$\mathbb{E}^{\text{Flexo}}_{IJK} := \frac{\partial^2 \bar{\Psi}^{\text{Flexo}}}{\partial \mathcal{E}_{IJ}\,\partial E_K} = J \mathfrak{C}_{KMIJ}\, \mu_{MABC}\, \mathcal{G}_{ABC}, \tag{B.16}$$

$$\mathbb{E}^{\text{Piezo}}_{IJK} := \frac{\partial^2 \bar{\Psi}^{\text{Piezo}}}{\partial \mathcal{E}_{IJ}\,\partial E_K} = J(\mathfrak{C}_{KMIJ}\, \eta_{MAB}\, \mathcal{E}_{AB} - C^{-1}_{KM}\, \eta_{MIJ}), \tag{B.17}$$

$$\mathbb{F}^{\text{Flexo}}_{IJKL} := \frac{\partial^2 \bar{\Psi}^{\text{Flexo}}}{\partial \mathcal{G}_{IJK}\,\partial E_L} = -J C^{-1}_{LM}\, \mu_{MIJK}, \tag{B.18}$$

$$\mathbb{G}^{\text{Elec}}_{IJKL} := \frac{\partial^2 \bar{\Psi}^{\text{Elec}}}{\partial \mathcal{E}_{IJ}\,\partial \mathcal{E}_{KL}} = \frac{1}{2} J \epsilon_0\, \mathscr{C}_{MFIJKL} E_M\, E_F, \tag{B.19}$$

$$\mathbb{H}^{\text{Elec}}_{IJK} := \frac{\partial^2 \bar{\Psi}^{\text{Elec}}}{\partial \mathcal{E}_{IJ}\,\partial E_K} = J \epsilon_0\, \mathfrak{C}_{KMIJ}\, E_M, \tag{B.20}$$

$$\mathbb{I}^{\text{Elec}}_{IJ} := \frac{\partial^2 \bar{\Psi}^{\text{Elec}}}{\partial E_I\,\partial E_J} = -J \epsilon_0\, C^{-1}_{IJ}, \tag{B.21}$$

with

$$\mathfrak{C}_{ABCD} := \frac{2}{J} \frac{\partial(-J C^{-1}_{AB})}{\partial C_{CD}} = C^{-1}_{AC} C^{-1}_{BD} + C^{-1}_{BC} C^{-1}_{AD} - C^{-1}_{AB} C^{-1}_{CD}, \tag{B.22}$$

$$\begin{aligned}\mathscr{C}_{ABCDEF} := \frac{2}{J} \frac{\partial(-J \mathfrak{C}_{ABCD})}{\partial C_{EF}} = &\mathscr{D}_{ACBDEF} + \mathscr{D}_{BDACEF} + \mathscr{D}_{ADBCEF} + \mathscr{D}_{BCADEF} - \mathscr{D}_{ABCDEF} \\ &- \mathscr{D}_{CDABEF},\end{aligned} \tag{B.23}$$

where

$$\mathscr{D}_{ACBDEF} := C^{-1}_{AB}\big(\frac{1}{2} C^{-1}_{CD} C^{-1}_{EF} - C^{-1}_{CE} C^{-1}_{DF} - C^{-1}_{CF} C^{-1}_{DE}\big). \tag{B.24}$$

Appendix C. Material model

Two material models, i.e. the isotropic Saint-Venant-Kirchhoff model and the isotropic Neo-Hookean model, are used to characterize the material properties in the numerical simulations. These models depend on the Lamé constants $\hat{\lambda}$ and $\hat{\mu}$ defined as

$$\hat{\lambda} = \frac{Y \nu}{(1+\nu)(1-2\nu)}, \quad \hat{\mu} = \frac{Y}{2(1+\nu)}. \tag{C.1}$$

For the isotropic Saint-Venant-Kirchhoff model, the elasticity energy density Ψ^{Elast} and its derivatives can be expressed as

$$\Psi^{\text{Elast}}(\boldsymbol{\mathcal{E}}) = \frac{\hat{\lambda}}{2} \operatorname{Tr}(\boldsymbol{\mathcal{E}})^2 + \hat{\mu} \operatorname{Tr}\left(\boldsymbol{\mathcal{E}}^2\right), \tag{C.2}$$

$$\frac{\partial \Psi^{\text{Elast}}(\boldsymbol{\mathcal{E}})}{\partial \mathcal{E}_{IJ}} = \hat{\lambda} \operatorname{Tr}(\boldsymbol{\mathcal{E}})\, \delta_{IJ} + 2\hat{\mu}\, \mathcal{E}_{IJ}, \tag{C.3}$$

$$\frac{\partial^2 \Psi^{\text{Elast}}(\boldsymbol{\mathcal{E}})}{\partial \mathcal{E}_{IJ} \partial \mathcal{E}_{KL}} = \hat{\lambda} \delta_{IJ} \delta_{KL} + 2\hat{\mu} \delta_{IK} \delta_{JL}. \tag{C.4}$$

For the isotropic Neo-Hookean model, the elasticity energy density Ψ^{Elast} and its derivatives can be expressed as

$$\Psi^{\text{Elast}}(\mathbf{C}) = \frac{\hat{\mu}}{2}\left(\text{Tr}(\mathbf{C}) - n_{\text{dim}}\right) - \hat{\mu}\ln(J) + \frac{\hat{\lambda}}{2}(\ln J)^2, \tag{C.5}$$

$$\frac{\partial \Psi^{\text{Elast}}(\mathbf{C})}{\partial \mathrm{C}_{IJ}} = \frac{\hat{\mu}}{2}\left(\delta_{IJ} - C^{-1}_{IJ}\right) + \frac{\hat{\lambda}}{2}\ln(J)\,C^{-1}_{IJ}, \tag{C.6}$$

$$\frac{\partial^2 \Psi^{\text{Elast}}(\mathbf{C})}{\partial \mathrm{C}_{IJ}\partial \mathrm{C}_{KL}} = \frac{1}{4}\left(\hat{\mu} - \hat{\lambda}\ln(J)\right)\left(C^{-1}_{IK}C^{-1}_{JL} + C^{-1}_{IL}C^{-1}_{JK}\right) + \frac{\hat{\lambda}}{4}C^{-1}_{IJ}C^{-1}_{KL}, \tag{C.7}$$

where n_{dim} denotes the dimension of the problem.

Data availability

No data was used for the research described in the article.

References

[1] B. Wang, Y. Gu, S. Zhang, et al., Flexoelectricity in solids: progress, challenges, and perspectives, Prog. Mater. Sci. 106 (2019) 100591, https://doi.org/10.1016/j.pmatsci.2019.05.003.
[2] W. Ma, L. Cross, Flexoelectricity of barium titanate, Appl. Phys. Lett. 88 (2006) 232902, https://doi.org/10.1063/1.2211309.
[3] M. Zelisko, Y. Hanlumyuang, S. Yang, et al., Anomalous piezoelectricity in two-dimensional graphene nitride nanosheets, Nat. Commun. 5 (2014) 4284, https://doi.org/10.1038/ncomms5284.
[4] J. Prost, P. Pershan, Flexoelectricity in nematic and smectic-a liquid crystals, J. Appl. Phys. 47 (1976) 2298–2312, https://doi.org/10.1063/1.323021.
[5] S. Baskaran, X. He, Q. Chen, et al., Experimental studies on the direct flexoelectric effect in α-phase polyvinylidene fluoride films, Appl. Phys. Lett. 98 (2011) 242901, https://doi.org/10.1063/1.3599520.
[6] A. Petrov, Flexoelectricity of model and living membranes, Biochim. Biophys. Acta, Biomembr. 1561 (2002) 1–25, https://doi.org/10.1016/S0304-4157(01)00007-7.
[7] K. Kim, S. Tadokoro, Electroactive polymers for robotic applications, in: Artif. Muscles Sens., vol. 23, 2007, p. 291.
[8] K. Kumar, P. Chen, H. Ren, A review of printable flexible and stretchable tactile sensors, Research (Wash. D C) 2019 (2019) 2730974, https://doi.org/10.34133/2019/3018568.
[9] Q. Deng, M. Kammoun, A. Erturk, et al., Nanoscale flexoelectric energy harvesting, Int. J. Solids Struct. 51 (2014) 3218–3225, https://doi.org/10.1016/j.ijsolstr.2014.05.018.
[10] R. Toupin, The elastic dielectric, J. Ration. Mech. Anal. 5 (1956) 849–915.
[11] R. Mindlin, Polarization gradient in elastic dielectrics, Int. J. Solids Struct. 4 (1968) 637–642, https://doi.org/10.1016/0020-7683(68)90079-6.
[12] R. Mindlin, N. Eshel, On first strain-gradient theories in linear elasticity, Int. J. Solids Struct. 4 (1968) 109–124, https://doi.org/10.1016/0020-7683(68)90036-X.
[13] S. Hu, S. Shen, Variational principles and governing equations in nano-dielectrics with the flexoelectric effect, Sci. China, Phys. Mech. Astron. 53 (2010) 1497–1504, https://doi.org/10.1007/s11433-010-4039-5.
[14] A. Hadjesfandiari, Size-dependent piezoelectricity, Int. J. Solids Struct. 50 (2013) 2781–2791, https://doi.org/10.1016/j.ijsolstr.2013.04.020.
[15] A. Li, S. Zhou, L. Qi, et al., A reformulated flexoelectric theory for isotropic dielectrics, J. Phys. D, Appl. Phys. 48 (2015) 465502, https://doi.org/10.1088/0022-3727/48/46/465502.
[16] R. Poya, A. Gil, R. Ortigosa, et al., On a family of numerical models for couple stress based flexoelectricity for continua and beams, J. Mech. Phys. Solids 125 (2019) 613–652, https://doi.org/10.1016/j.jmps.2019.01.013.
[17] S.S. Nanthakumar, X. Zhuang, H.S. Park, et al., Topology optimization of flexoelectric structures, J. Mech. Phys. Solids 105 (2017) 217–234, https://doi.org/10.1016/j.jmps.2017.05.010.
[18] D. Codony, A. Mocci, J. Barceló-Mercader, et al., Mathematical and computational modeling of flexoelectricity, J. Appl. Phys. 130 (2021) 231101, https://doi.org/10.1063/5.0067852.
[19] L. Liu, An energy formulation of continuum magneto-electro-elasticity with applications, J. Mech. Phys. Solids 63 (2014) 451–480, https://doi.org/10.1016/j.jmps.2013.08.001.
[20] Q. Deng, L. Liu, P. Sharma, Chapter 3 a continuum theory of flexoelectricity, in: A. Tagantsev, P. Yudin (Eds.), Flexoelectricity in Solids: From Theory to Applications, World Scientific, 2016, pp. 43–74.
[21] J. Yvonnet, L. Liu, A numerical framework for modeling flexoelectricity and Maxwell stress in soft dielectrics at finite strains, Comput. Methods Appl. Mech. Eng. 313 (2017) 450–482, https://doi.org/10.1016/j.cma.2016.09.007.
[22] T. Thai, T. Rabczuk, X. Zhuang, A large deformation isogeometric approach for flexoelectricity and soft materials, Comput. Methods Appl. Mech. Eng. 341 (2018) 718–739, https://doi.org/10.1016/j.cma.2018.05.019.
[23] D. Codony, P. Gupta, O. Marco, et al., Modeling flexoelectricity in soft dielectrics at finite deformation, J. Mech. Phys. Solids 146 (2021) 104182, https://doi.org/10.1016/j.jmps.2020.104182.
[24] F. Deng, W. Yu, X. Liang, et al., A mixed finite element method for large deformation of flexoelectric materials, Appl. Math. Model. 118 (2023) 1034–1053, https://doi.org/10.1016/j.apm.2023.01.029.
[25] X. Zhuang, T.Q. Thai, T. Rabczuk, Topology optimization of nonlinear flexoelectric structures, J. Mech. Phys. Solids (2022) 105117, https://doi.org/10.1016/j.jmps.2022.105117.
[26] T.Q. Thai, X. Zhuang, H.S. Park, et al., A staggered explicit-implicit isogeometric formulation for large deformation flexoelectricity, Eng. Anal. Bound. Elem. 122 (2021) 1–12, https://doi.org/10.1016/j.enganabound.2020.10.004.
[27] L. Dorfmann, R. Ogden, Nonlinear Theory of Electroelastic and Magnetoelastic Interactions, vol. 1, Springer, New York, 2014.
[28] R. Pelrine, R. Kornbluh, Q. Pei, et al., High-speed electrically actuated elastomers with strain greater than 100%, Science 287 (2000) 836–839, https://doi.org/10.1126/science.287.5454.836.
[29] J. Plante, S. Dubowsky, Large-scale failure modes of dielectric elastomer actuators, Int. J. Solids Struct. 43 (2006) 7727–7751, https://doi.org/10.1016/j.ijsolstr.2006.03.026.
[30] R. Sahu, A. Saini, D. Ahmad, et al., Estimation and validation of Maxwell stress of planar dielectric elastomer actuators, J. Mech. Sci. Technol. 30 (2016) 429–436, https://doi.org/10.1007/s12206-015-1247-y.

[31] R. Bustamante, A. Dorfmann, R. Ogden, Nonlinear electroelastostatics: a variational framework, Z. Angew. Math. Phys. 60 (2009) 154–177, https://doi.org/10.1007/s00033-007-7145-0.
[32] J.C. Maxwell, Viii. A dynamical theory of the electromagnetic field, Philos. Trans. R. Soc. Lond. 155 (1865) 459–512.
[33] H. Lorentz, The Theory of Electrons and Its Applications to the Phenomena of Light and Radiant Heat, Columbia University Press, New York, 1909, a Course of Lectures Delivered in Columbia University, New York, in March and April 1906.
[34] H. Minkowski, Die Grundgleichungen für die elektromagnetischen Vorgänge in bewegten Körpern, Nachr. Ges. Wiss. Gött., Math.-Phys. Kl. 1908 (1908) 53–111, https://doi.org/10.1007/BF01455871.
[35] M. Abraham, Zur Frage der Symmetrie des elektromagnetischen Spannungstensors, Ann. Phys. (Leipz.) 349 (1914) 537–544, https://doi.org/10.1002/andp.19143491204.
[36] A. Einstein, J. Laub, Über die ponderomotive Kräfte, die auf ruhende Körper im elektromagnetischen Felde ausgeübt werden, Ann. Phys. (Leipz.) 331 (1908) 541–550, https://doi.org/10.1002/andp.19083310807.
[37] A. Schlosser, L. Behlen, A. Ricoeur, Electrostatic body forces in cracked dielectrics and their implication on Maxwell stress tensors, Contin. Mech. Thermodyn. 36 (4) (2024) 877–890, https://doi.org/10.1007/s00161-024-01302-7.
[38] H. Zhang, F. Wang, B. Nestler, Multi-component electro-hydro-thermodynamic model with phase-field method. i. Dielectric, J. Comput. Phys. 505 (2024) 112907, https://doi.org/10.1016/j.jcp.2024.112907.
[39] J. Pelteret, D. Davydov, A. McBride, et al., Computational electro-elasticity and magneto-elasticity for quasi-incompressible media immersed in free space, Int. J. Numer. Methods Eng. 108 (2016) 1307–1342, https://doi.org/10.1002/nme.5254.
[40] G. Kofod, P. Sommer-Larsen, Silicone dielectric elastomer actuators: finite-elasticity model of actuation, Sens. Actuators A, Phys. 122 (2005) 273–283, https://doi.org/10.1016/j.sna.2005.05.001.
[41] P. Saxena, J. Pelteret, P. Steinmann, Modelling of iron-filled magneto-active polymers with a dispersed chain-like microstructure, Eur. J. Mech. A Solids 50 (2015) 132–151, https://doi.org/10.1016/j.euromechsol.2014.10.005.
[42] D. Vu, P. Steinmann, A 2-D coupled BEM-FEM simulation of electro-elastostatics at large strain, Comput. Methods Appl. Mech. Eng. 199 (2010) 1124–1133, https://doi.org/10.1016/j.cma.2009.12.001.
[43] D. Vu, P. Steinmann, On 3-D coupled BEM–FEM simulation of nonlinear electro-elastostatics, Comput. Methods Appl. Mech. Eng. 201–204 (2012) 82–90, https://doi.org/10.1016/j.cma.2011.08.024.
[44] C. Dev, G. Stankiewicz, P. Steinmann, On the influence of free space in topology optimization of electro-active polymers, Struct. Multidiscip. Optim. 66 (2023) 196, https://doi.org/10.1007/s00158-023-03634-5.
[45] A. Abdollahi, C. Peco, D. Millán, et al., Computational evaluation of the flexoelectric effect in dielectric solids, J. Appl. Phys. 116 (2014) 094309, https://doi.org/10.1063/1.4893974.
[46] A. Abdollahi, D. Millán, C. Peco, et al., Revisiting pyramid compression to quantify flexoelectricity: a three-dimensional simulation study, Phys. Rev. B 91 (2015) 104103, https://doi.org/10.1103/PhysRevB.91.104103.
[47] B. He, B. Javvaji, X. Zhuang, Characterizing flexoelectricity in composite material using the element-free Galerkin method, Energies 12 (2019) 271, https://doi.org/10.3390/en12020271.
[48] X. Zhuang, S. Nanthakumar, T. Rabczuk, A meshfree formulation for large deformation analysis of flexoelectric structures accounting for the surface effects, Eng. Anal. Bound. Elem. 120 (2020) 153–165, https://doi.org/10.1016/j.enganabound.2020.07.021.
[49] S. Mao, P. Purohit, N. Aravas, Mixed finite-element formulations in piezoelectricity and flexoelectricity, Proc. Royal Soc. A 472 (2016) 20150879, https://doi.org/10.1098/rspa.2015.0879.
[50] F. Deng, Q. Deng, W. Yu, et al., Mixed finite elements for flexoelectric solids, J. Appl. Mech. 84 (2017) 081004, https://doi.org/10.1115/1.4036939.
[51] S. Nanthakumar, X. Zhuang, H. Park, et al., Topology optimization of flexoelectric structures, J. Mech. Phys. Solids 105 (2017) 217–234, https://doi.org/10.1016/j.jmps.2017.05.010.
[52] X. Tian, J. Sladek, V. Sladek, et al., A collocation mixed finite element method for the analysis of flexoelectric solids, Int. J. Solids Struct. 217–218 (2021) 27–39, https://doi.org/10.1016/j.ijsolstr.2021.01.031.
[53] H. Ghasemi, H. Park, X. Zhuang, et al., Three-dimensional isogeometric analysis of flexoelectricity with Matlab implementation, Comput. Mater. Continua 65 (2020) 1157–1179, https://doi.org/10.32604/cmc.2020.08358.
[54] X. Chen, S. Yao, J. Yvonnet, Dynamic analysis of flexoelectric systems in the frequency domain with isogeometric analysis, Comput. Mech. 71 (2023) 1127–1148, https://doi.org/10.1007/s00466-022-02244-0.
[55] X. Zhuang, B. Nguyen, S. Nanthakumar, et al., Computational modeling of flexoelectricity-a review, Energies 13 (2020) 1326, https://doi.org/10.3390/en13061326.
[56] D. Codony, O. Marco, S. Fernández-Méndez, et al., An immersed boundary hierarchical B-spline method for flexoelectricity, Comput. Methods Appl. Mech. Eng. 354 (2019) 750–782, https://doi.org/10.1016/j.cma.2019.05.036.
[57] A. McBride, D. Davydov, P. Steinmann, Modelling the flexoelectric effect in solids: a micromorphic approach, Comput. Methods Appl. Mech. Eng. 371 (2020) 113320, https://doi.org/10.1016/j.cma.2020.113320.
[58] H. Atef, A. El-Dhaba, Modeling the flexoelectric effect via the reduced micromorphic model, Compos. Struct. 290 (2022) 115504, https://doi.org/10.1016/j.compstruct.2022.115504.
[59] D. Vu, P. Steinmann, On the spatial and material motion problems in nonlinear electro-elastostatics with consideration of free space, Math. Mech. Solids 17 (2012) 803–823, https://doi.org/10.1177/1081286511430161.
[60] R. Bustamante, A. Dorfmann, R. Ogden, On electric body forces and Maxwell stresses in nonlinearly electroelastic solids, Int. J. Eng. Sci. 47 (2009) 1131–1141, https://doi.org/10.1016/j.ijengsci.2008.10.010.
[61] X. Du, G. Zhao, W. Wang, et al., NLIGA: a Matlab framework for nonlinear isogeometric analysis, Comput. Aided Geom. Des. 80 (2020) 101869, https://doi.org/10.1016/j.cagd.2020.101869.
[62] M. Majdoub, P. Sharma, T. Çağin, Erratum: enhanced size-dependent piezoelectricity and elasticity in nanostructures due to the flexoelectric effect [Phys. Rev. B 77 (2008) 125424], Phys. Rev. B 79 (2009) 119904, https://doi.org/10.1103/PhysRevB.79.119904.
[63] E. Bursian, O. Zaikovsk, Changes in curvature of a ferroelectric film due to polarization, Sov. Phys., Solid State 10 (1968) 1121.
[64] R. Ortigosa, J. Martínez-Frutos, D. Ruiz, et al., Density-based topology optimisation considering nonlinear electromechanics, Struct. Multidiscip. Optim. 64 (2021) 257–280, https://doi.org/10.1007/s00158-021-02886-3.
[65] X. Zhao, W. Hong, Z. Suo, Electromechanical hysteresis and coexistent states in dielectric elastomers, Phys. Rev. B 76 (2007) 134113, https://doi.org/10.1103/PhysRevB.76.134113.
[66] Q. Wang, Z. Suo, X. Zhao, Bursting drops in solid dielectrics caused by high voltages, Nat. Commun. 3 (2012) 1153, https://doi.org/10.1038/ncomms2178.
[67] S. Seifi, H. Park, Computational modeling of electro-elasto-capillary phenomena in dielectric elastomers, Int. J. Solids Struct. 87 (2016) 236–244, https://doi.org/10.1016/j.ijsolstr.2016.02.004.
[68] S. Seifi, K. Park, H. Park, A staggered explicit–implicit finite element formulation for electroactive polymers, Comput. Methods Appl. Mech. Eng. 337 (2018) 150–164, https://doi.org/10.1016/j.cma.2018.03.028.
[69] S. Torza, R. Cox, S. Mason, Electrohydrodynamic deformation and bursts of liquid drops, Philos. Trans. R. Soc. A 269 (1971) 295–319, https://doi.org/10.1098/rsta.1971.0032.

Xiaoying Zhuang is Heisenberg Professor and Chair of Computational Science and Simulation Technology at Leibniz University Hannover. She obtained her PhD from Durham University 3D fracture modeling in 2011. Her research combines computational mechanics and machine learning to design advanced materials such as metamaterials, nanostructures, and 2D materials. As a highly cited researcher, she has been rewarded with numerous awards including Sofja Kovalevskaja Award, ERC Starting Grant, Heinz Maier-Leibnitz Prize, K.J. Bathe Award, and Qidi Prize. Her current projects focus on nano-energy harvesters (ERC-funded) and machine learning-driven design of next-generation 2D materials and metamaterials.